Biophysical *Journal*
Article

Biophysical Society

GsMTx4: Mechanism of Inhibiting Mechanosensitive Ion Channels

Radhakrishnan Gnanasambandam,[1] Chiranjib Ghatak,[2] Anthony Yasmann,[3] Kazuhisa Nishizawa,[4]
Frederick Sachs,[1] Alexey S. Ladokhin,[2] Sergei I. Sukharev,[3] and Thomas M. Suchyna[1,*]
[1]Department of Physiology and Biophysics, State University of New York, Buffalo, New York; [2]Department of Biochemistry and Molecular Biology, University of Kansas Medical Center, Kansas City, Kansas; [3]Department of Biology, University of Maryland, College Park, Maryland; and [4]Clinical Laboratory Science, Teikyo University School of Medical Technology, Tokyo, Japan

ABSTRACT GsMTx4 is a spider venom peptide that inhibits cationic mechanosensitive channels (MSCs). It has six lysine residues that have been proposed to affect membrane binding. We synthesized six analogs with single lysine-to-glutamate substitutions and tested them against Piezo1 channels in outside-out patches and independently measured lipid binding. Four analogs had ~20% lower efficacy than the wild-type (WT) peptide. The equilibrium constants calculated from the rates of inhibition and washout did not correlate with the changes in inhibition. The lipid association strength of the WT GsMTx4 and the analogs was determined by tryptophan autofluorescence quenching and isothermal calorimetry with membrane vesicles and showed no significant differences in binding energy. Tryptophan fluorescence-quenching assays showed that both WT and analog peptides bound superficially near the lipid-water interface, although analogs penetrated deeper. Peptide-lipid association, as a function of lipid surface pressure, was investigated in Langmuir monolayers. The peptides occupied a large fraction of the expanded monolayer area, but that fraction was reduced by peptide expulsion as the pressure approached the monolayer-bilayer equivalence pressure. Analogs with compromised efficacy had pressure-area isotherms with steeper slopes in this region, suggesting tighter peptide association. The pressure-dependent redistribution of peptide between "deep" and "shallow" binding modes was supported by molecular dynamics (MD) simulations of the peptide-monolayer system under different area constraints. These data suggest a model placing GsMTx4 at the membrane surface, where it is stabilized by the lysines, and occupying a small fraction of the surface area in unstressed membranes. When applied tension reduces lateral pressure in the lipids, the peptides penetrate deeper acting as "area reservoirs" leading to partial relaxation of the outer monolayer, thereby reducing the effective magnitude of stimulus acting on the MSC gate.

INTRODUCTION

GsMTx4 is a gating modifier peptide from spider venom (1,2), notable for its selective inhibition of cation-permeable mechanosensitive channels (MSCs) belonging to the Piezo (3) and TRP (4,5) channel families. It has become an important pharmacological tool for identifying the role of these excitatory MSCs in normal physiology and pathology (6–8). GsMTx4 is similar to many other channel-active peptides isolated from spider venom, which are small (3–5 kD) amphipathic molecules built on a conserved inhibitory cysteine-knot (ICK) backbone (9). However, it is unique because 1) of its high potency for inhibiting mechanosensitive channels and 2) inhibition by GsMTx4 is not stereospecific, i.e., both its enantiomers (L- and D-form) inhibit MSCs (1), a feature not observed with other ICK peptides (10).

All ICK peptides are amphipathic, having a hydrophobic face that can promote interfacial adsorption to the lipid bilayer (10,11). In the membrane-absorbed state, many of these peptides modify channel kinetics (1,12) by directly binding to channel gating elements (13–15) rather than occluding the channel pore. GsMTx4's lack of stereospecificity, but local effect on the channel (within a Debye length of the channel pore), suggests a different mechanism of inhibition than other ICK peptides. MSCs, like Piezo channels, appear to be activated by bilayer tension (16), and tension modulates bilayer density (17) and thickness (18). This prompted the current model of GsMTx4 inhibition, suggesting it acts by modulating local membrane tension

---

Submitted June 10, 2016, and accepted for publication November 3, 2016.

*Correspondence: suchyna@buffalo.edu

Radhakrishnan Gnanasambandam, Chiranjib Ghatak, and Anthony Yasmann contributed equally to this work.

Frederick Sachs, Alexey S. Ladokhin, Sergei I. Sukharev, and Thomas M. Suchyna contributed equally to this work.

Editor: Paulo Almeida
http://dx.doi.org/10.1016/j.bpj.2016.11.013

near the MSCs. However, because all ICK peptides are amphipathic, we wanted to know why GsMTx4 is more potent at inhibiting MSCs.

GsMTx4 is highly positively charged (+5) (19) compared with other ICK peptides, primarily because of its six lysine residues. However, surprisingly, it only has a weak preference for anionic over zwitterionic lipids (11). Other ICK peptides, like GsMTx1 and SGTx1, with lower net positive charge (+3), show a strong preference for anionic lipids. Despite GsMTx4's weak selectivity for anionic lipids, its partitioning energies were comparable with the peptides cited above (11,20). GsMTx4's high energy of partitioning into either lipid type may be associated with its relatively high hydrophobicity and lysine content compared with other ICK peptides; lysine plays an important role in peptide-lipid interactions (21,22).

Partitioning energies are only one factor affecting inhibition of channels by ICK peptides. The depth of peptide penetration following absorption is an important modulator of interactions with both intramembrane and extracellular gating elements (23), and the depth of penetration is dependent on membrane tension (24). Based on molecular dynamics (MD) modeling, two binding modes have been suggested for how GsMTx4 is positioned in the bilayer. In one mode, there is an energy minima at the interfacial boundary (25–29). A second less-occupied mode was found where the peptides bound deeper and interacted with both monolayers simultaneously (27,29,30). Although GsMTx4 can occupy both of these modes, the simulations suggest it is less likely to occupy the deeper mode than other ICK peptides (25,30). The relatively stronger interaction of GsMTx4 with the membrane interface may inhibit occupancy of the deeper mode in relaxed bilayers (25,29,30).

Although the hydrophobic face of ICK peptides is clearly important for membrane insertion, the role played by GsMTx4's high lysine content could be important as well. MD simulations suggest the positive charge on GsMTx4 is critical in setting the depth of penetration and the lipid displacement (29). We experimentally investigated the role of charge by synthesizing six different lysine to glutamate (K-E) analogs, resulting in a net charge reduction to +3 compared with the +5 on the wild-type (WT). The functional differences among the K-E analogs were determined by the magnitude and kinetics of their inhibition of Piezo1 channels. Four of these analogs showed compromised steady-state inhibition that was *not* due to changes in the kinetics of inhibition or the lipid partitioning energies. However, using different lipid binding assays, we found that all peptides bound superficially to bilayers but penetrated deeper in expanded monolayers, occupying greater surface area and producing a "tension clamping" effect. The four compromised analogs showed reduced expulsion as the monolayer was compressed, thus reducing the area reservoir for tension clamping. To our knowledge, these results support a new model of peptide inhibition where 1) the distribution of charges influences GsMTx4's orientation and depth in the relaxed membranes and 2) the equilibrium between shallow and more deeply bound modes is dependent on bilayer tension changes (17).

MATERIALS AND METHODS

Peptide synthesis and folding

The WT GsMTx4 (synthetic L amino acid form) and lysine to glutamate substituted analogs were chemically synthesized and folded by CSBio (Menlo Park, CA) according to published procedures (19). Six analog peptides were generated, which we called K8E, K15E, K20E, K22E, K25E, and K28E.

Circular dichroism

Circular dichroism (CD) measurements were performed on peptides at 2 μM using an upgraded Jasco-720 spectropolarimeter (Japan Spectroscopic, Tokyo, Japan). Normally 80–100 scans were recorded to increase the signal-to-noise ratio at 200–260 nm using a 1 nm optical path. Spectra were corrected for background scattering by subtracting a vesicle-only spectra. Temperature was controlled by a Peltier unit.

Electrophysiology

Human embryonic kidney cell (HEK)293 cells were transfected with 0.5–1 μg of mouse Piezo1 cDNA expression vector that coexpressed Green Fluorescent Protein (GFP; gift from A. Patapoutian, Scripps Research Institute, La Jolla, CA) (3). Mechanically activated currents were recorded from outside-out patches with an Axopatch 200B amplifier (Axon Instruments, Sunnyvale, CA). An HSPC-1 pressure clamp (ALA Scientific Instruments, Farmingdale, NY) was used to apply the stimulus that consisted of a train of 500 ms positive pressure steps separated by 1500 ms relaxation intervals. We analyzed Piezo patch currents that showed consistent responses within 40–90 mmHg. This range showed the most consistent activation of currents despite some variability in factors such as patch diameter and extent of cytoskeletal disruption (31). Integrated current (i.e., the total charge transferred) was used because this measure tended to smooth the data between pressure steps compared with the large step-to-step variations observed in peak current measurements. Outside-out patch formation also caused labile Piezo inactivation so we did not analyze the inactivation kinetics. From observing more than 100 outside-out patch currents, none of the analogs showed an obvious effect on inactivation kinetics. Individual peptides were superfused onto the patches using an ALA MP285 perfusion system. Electrical recordings (data were acquired at 10 kHz and filtered online at 2 kHz), stimulus generation, and peptide applications were controlled by QuBio software, and analyzed using QuB Express (http://www.qub.buffalo.edu/wiki/index.php/QUB_Express) and Origin 8.5. For Piezo1 channels, the extracellular solution contained 145 mM NaCl, 5 mM KCl, 3 mM $MgCl_2$, 0.1 mM $CaCl_2$, and 10 mM HEPES (pH 7.4). The pipette solution contained 133 mM CsCl, 10 mM HEPES (pH 7.4). The inhibition produced by application of the peptides was followed by ~60 s of washout, followed by application of WT GsMTx4 as a control. Peptide solutions were made fresh daily, and the peptide concentration emerging from the perfusion tip was sampled and quantified with an Agilent (Santa Clara, CA) 1100 series HPLC before use.

Kinetic rate constants and KD calculation

We modeled the current decay and recovery rates with either double or single exponential equations, respectively (see Fig. 2 *B*). These rates were used to calculate the association (k_a) and dissociation (k_d) constants (see Fig. 2 *D*). The k_{a1} values shown in Fig. 2 *D* are calculated from the shorter time constants that represented >80% of the total reduction in current amplitude (both WT and analogs). There were no statistical differences in the k_{a2} values calculated from the longer time constants (Fig. S5 in the Supporting Material). The ratio of k_{a1}/k_d for each peptide was used to calculate the effective equilibrium dissociation constant (K_D, see Fig. 2 *E*).

Statistics

The goodness of the exponential fits to the decay and recovery phases for individual patches were assessed using the value-adjusted *r*-square in Origin 8.5 software, and time constants from fits with $R^2 > 0.7$ were used to calculate the association (k_a) and dissociation (k_d) constants. This generally included >90% of the patches tested. The k_a and k_d from multiple patches were averaged for each analog and statistically different values for analogs versus WT constants were evaluated by one-way ANOVA using both the Tukey and Bonferroni test methods ($\alpha = 0.05$). We determined the 90% confidence intervals and calculated SE for the k_d/k_a ratio (the effective equilibrium constants (K_D)) using Fieller's method (32) where the means for k_a and k_d approximated Gaussian distributions. Statistically significant differences between the percent channel inhibition for the WT and analog peptides was evaluated by one-way ANOVA ($\alpha = 0.05$).

Fluorescence measurements of membrane penetration

The interaction between these tryptophan-containing peptides and lipid vesicles was studied as described in (33). Briefly, 2 μM peptide was dissolved in 10 mM $NaPO_4$ buffer (pH 7.4). Tryptophan (Trp) fluorescence was measured using a SPEX Flurolog FL 3-22 steady-state fluorescence spectrometer (Jobin Yvon, Edison, NJ) equipped with double-grating excitation and emission monochromators. Trp residues were excited at 280 nm and emission spectra were recorded between 290 and 500 nm using excitation and emission spectral slits of 2 and 4 nm, respectively. For acrylamide quenching, 295 nm excitation was used to reduce inner filter effects. Measurements were made at 25°C in 2 × 10 mm cuvettes oriented perpendicular to the excitation beam. Quenching of Trp emission was measured in the presence of large unilamellar vesicles (LUVs) composed of 1-palmitoyl-2-oleoyl-sn-glycero-3-phosphocholine (POPC) and 1-palmitoyl-2-oleoyl-sn-glycero-3-phosphoglycerol (POPG) (Avanti Polar Lipids, Alabaster, AL). All spectra were recorded after equilibration of the sample. Corrections for background and the fitting of spectra were performed as previously described (34). It should be noted that, due to peptide aggregation, a two-state model (transitions between soluble and membrane bound pools) is insufficient to explain the differences in the peak and absolute Trp fluorescence intensity. Shifts in the peak fluorescence and changes in I_{max} are likely a combination of transitioning among multimer, monomer, and membrane-associated pools, each with unique Trp fluorescence quenching properties. However, the mole fraction partition coefficient is not dependent on the absolute I_{max} value (33), so we were able to calculate the free energy of partitioning from the relative fluorescence intensity changes upon lipid titration.

For depth-dependent quenching we used a series of brominated lipids (Avanti Polar Lipids) at positions 6,7; 9,10; and 11,12 along one of the acyl chains (6,7; 9,10; and 11,12-brominated phosphatidylcholine (BrPCs)). Depth-dependent quenching profiles were generated by taking the ratio of tryptophan intensity *F*, to that in the absence of quenchers, F_0, as a function of the depth of the bromine. Because the maxima of the quenching profile are shallower than the depths of available bromolipids, we used a priori constraints to estimate the depth. We used the method of distribution analysis (35,36) that approximates the quenching profile as Gaussian. Because the quenching profile is poorly defined, no unique solution exists when all three fitting parameters are varied. One can estimate the average position assuming a particular width of the distribution. Based on our previous experience with quenching of various peptides, we assumed a value of 5 Å for the dispersion of the Gaussian distribution (37). Note, that narrower distributions would be inconsistent with the presence of the two neighboring tryptophan residues whereas a wider distribution would have little effect on our conclusions.

Langmuir monolayer experiments

All experiments were conducted in a buffer made with 50 mM KCl, 10 mM KPi, titrated to pH 7.2. In both liposome and monolayer experiments, the lipids were composed of POPG-POPC (3:1 mol/mole). The peptides were dissolved into buffer to make stock solutions of 150 μM and then stored for no more than 2 days at 4°C; samples were never frozen. Langmuir monolayer experiments were done with a two-barrier, rectangular (22 × 6 cm) trough (Kibron MicroTrough XS; Helsinki, Finland) housed in an AirClean enclosure. A Dyneprobe (Kibron) metal alloy needle was used as the Wilhelmy plate. A POPG-POPC mixture (both from Avanti Polar Lipids) was dissolved in chloroform to a final concentration of 0.2 mg/ml. The lipids were deposited onto the subphase using a gastight 50 μL Hamilton syringe; the measurements were started after 10 min to allow the solvent to evaporate. Pressure/area (π-*A*) isotherms of monolayers were measured at room temperature (~20°C) from 114 to 18 cm^2 at a barrier rate of 20 mm/min. For each analog, isotherms were measured at least three times. The inverse lateral compressibility moduli $Cs^{-1} = A(d\pi/dA)$ were determined from the isotherms (38).

Isothermal titration calorimetry

POPG-POPC (3:1) liposomes were prepared by rehydrating 2 mg of dried lipid mixture in a round-bottom glass tube with buffer made with 50 mM KCl, 10 mM KPi, titrated to pH 7.2. They were then vortexed and sonicated in a Branson-type bath sonicator for 1 min. Isothermal calorimetry (ITC) experiments were carried out using a Microcal (Malvern Instruments, Malvern, UK) VP-ITC Microcalorimeter. The heat of the high peptide dilution predefined the titration configuration in which 10–30 μM peptide was in the cell and a 0.3–1 mM liposome suspension was in the syringe. Injections of 20 μL were spaced by 300 s intervals. For all peptides, interactions with POPG-POPC liposomes were exothermic. After minor baseline adjustments, the thermograms were fitted with single-site binding curves to determine the mean parameters (usually defined by the major low-affinity population of sites). Then, guided by this fit, we fit to a two-site model. The two-site fittings were significantly better suggesting the presence of a second, higher affinity population of sites.

Simulations of GsMTx4 interaction with monolayer

For the POPC monolayer simulations, the united-atom parameters GROMOS53A6 (39) for protein and GROMOS53A6$_L$ (40) for POPC were used. The simulation programs, conditions and H_2O models were basically the same as those used in (41), except for the surface tension coupling used to control the pressure of the monolayer. The system was comprised of a monolayer of 40 POPC, one peptide (WT or K15E) and 1460 H_2O along with Cl ions that neutralized the positive charges of the peptides. The basic configuration of the system was similar to the previous reports (42,43). Twenty different initial structures were prepared using the bilayer/peptide structures randomly sampled from our recent 400 ns trajectories with bilayers (41) and initially subjected to a 50 ns run with the surface tension (γ_s) coupling at 50 mN/m that brought the area per lipid to ~0.64 nm^2 in the monolayer. These twenty runs for both WT and K15E were continued with 20 mN/m stepwise increases and decreases in the target value of γ_s, i.e., 70 and 90 mN/m, and 30, 10, 0, and −10 mN/m runs, respectively, with the time length being 40 ns for each except for the run with γ_s,$= -10$ mN/m, which was extended to 100 ns. This procedure controlled γ_s with precision of SD < 0.1 mN/m in all cases. The final 20 ns of each run were used to compute the monolayer area and the peptide height (*z*-position of the center of mass). Due to this relatively short equilibration period at each tension value, we acknowledge that our simulation data, shown in Fig. 7, should rather be regarded as a qualitative one, which needs to be reexamined using longer equilibration runs (e.g., ~1 μs). For the height analysis, POPC phosphorus atoms were used as the references, but the phosphorus atoms located within 1 nm of any peptide atoms were not used due to local perturbation of lipids headgroups specific to the peptides that made the WT-versus-K15E comparison difficult.

Of note, it is not straightforward to compare the computed surface tension γ_s with the absolute experimental π values. In theory, the following formula allows us to convert γ_s to π: $\pi = \gamma_{wv} - \gamma_m$ and the $\gamma_m = \gamma_s - \gamma_{wv}$, where, γ_m is the monolayer/water interfacial tension and γ_{wv} is the surface tension at the water/vacuum interface (44). However, the simulated surface tensions at the water/vacuum interface actually differ considerably from the experimental values due to defects in the water models (43). To better compare the γ_s-area curve with the experimental π-area curve, we chose the method described in Baoukina et al. (43), with which correction to the γ_{wv} was introduced to obtain an effective γ_{wv}* so that the two curves can be compared. We compared our computed γ_s-area curve with the experimental curve of a POPC monolayer (45) and chose $\gamma_{wv}^* = 45$ mN/m to convert γ_s to the effective monolayer pressure π_{eff}. This choice was close to the suggestion of 47 mN/m based on the dipalmitoylphosphatidylcholine (DPPC) simulations (43).

RESULTS

Structural analysis of lysine analogs

At a pH of 7.4, lysine residues are protonated and contribute substantially to the net positive charge on GsMTx4. MD simulations predict electrostatic interactions between the lysine residues and the carbonyl/phosphates of lipid head groups (25,29). We made six single substitutions of lysine-to-glutamate generating analogs with a net charge of +3. Mass spectrometry confirmed the formation of peptides of expected mass containing three disulfide bonds. As an additional check of the secondary structure, we measured the CD spectra of the peptides. The L-GsMTx4 spectrum was relatively unchanged by the addition of either 100% POPC (zwitterionic) or 3:1 POPG:POPC (negatively charged) LUVs. A general increase in intensity was observed when bound to POPG:POPC, likely due to stabilization of the secondary structure (Fig. S1 *A*). The spectrum of D-GsMTx4, which is inverted with respect to that of L-GsMTx4, is also shown. The in-solution spectrum of the WT was similar at all wavelengths to that of the analogs except for a distinct negative peak at ~228 nm for every analog (Fig. 1 *A*). However, the spectra of the WT and analogs in POPG:POPC LUVs were similar and lacked the 228 nm peak (Fig. 1 *B*). The peak reappeared when the analogs were added to POPC LUVs (Fig. S1 *B*). The 228 nm peak may arise from the formation of aggregates due to interpeptide hydrophobic interactions in solution or when weakly bound to membranes (see Figs. S2 and S3). If so, then a strong association with negatively charged membranes, such as the POPG:POPC LUVs, may dissociate aggregates.

Functional analysis of MSC inhibition

All of the peptides (5 μM) were tested on outside-out patches from HEK cells transfected with mouse Piezo1 cDNA (Fig. 2). We measured the charge transfer (integrated current over the entire pressure step) elicited by the pressure steps before, during perfusion with ~5 μM peptide (until the charge transfer reached steady-state), and during washout (Fig. 2 *B*). Charge transfer recovery during washout did not return to 100% due to channel rundown, but the recovery level was similar for all analogs and

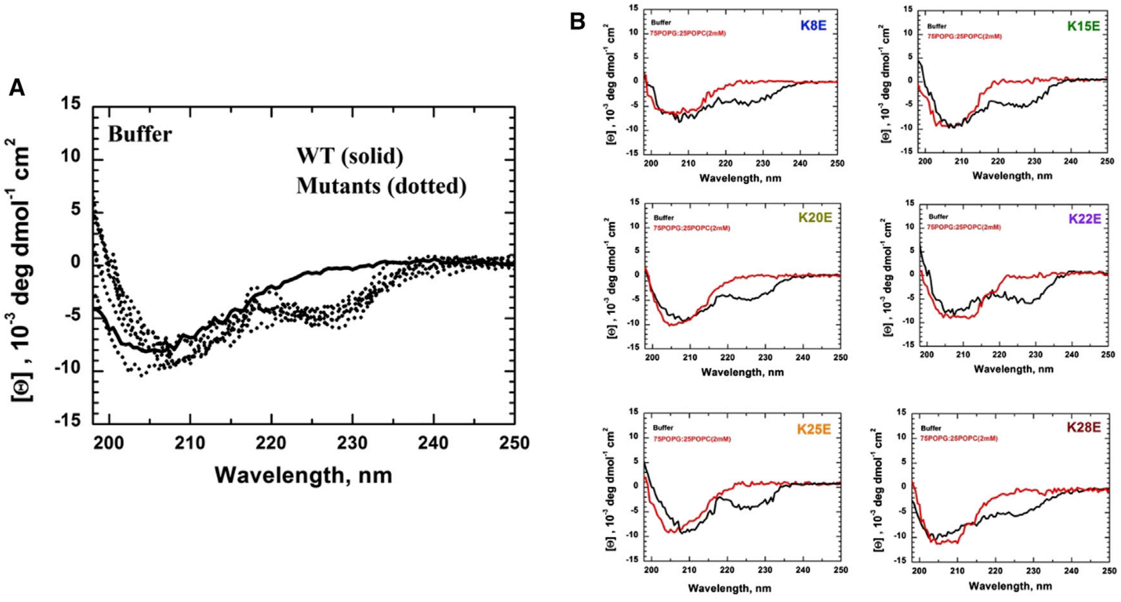

FIGURE 1 (*A*) Representative CD spectrum from all GsMTx4 peptides (2 μM) shows a distinct negative peak at 228 nm for all K-E analogs compared with WT. Other regions of the spectrum are similar to WT. (*B*) CD spectra before and after binding to negatively charged POPG-POPC lipid vesicles is shown. When bound, the 228 nm peak disappears and the spectrum more closely resembles that of the WT. To see this figure in color, go online.

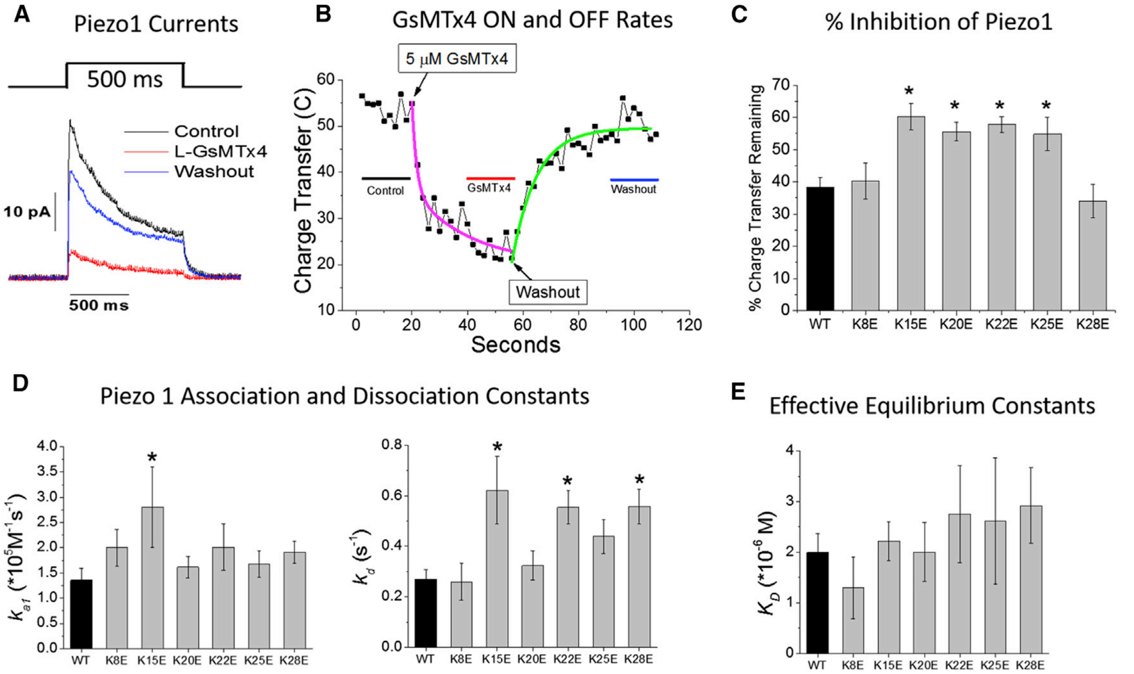

FIGURE 2 (*A*) Typical averaged currents in an outside-out patch from a cell expressing Piezo1, before (*black*), during (*red*), and after (*blue*) application of 5 μM WT GsMTx4. Patch currents were recorded at -50 mV pipette potential. (*B*) A typical experiment (not the same as *A*) shows the integrated current (charge transfer) levels diminishing over time after GsMTx4 application and recovering after washout. The regions from which the charge transfer levels were determined are indicated by lines in (*B*) with colors coordinated to the traces in (*A*). The mean reduction of Piezo 1 charge transfer by the different peptides is shown in (*C*). The average charge transfer from the 500 ms steps before peptide application (*control line* in *B*) were set to 100% to normalize the inhibition of different patches. The percent values in (*C*) represent the average fractional reduction in steady-state charge-transfer determined from the region indicated by the red line in (*B*). For a summary of individual patch data, see Fig. S4. Asterisks represent significantly different means at $\alpha = 0.05$. Time constants were determined by modeling the decay and recovery phases with exponential fits (*magenta and green curves*, respectively, in *B*). The net association (k_a) and dissociation (k_d) rate constants for inhibition of Piezo1 (*D*) were calculated from the first-order time constants derived from the exponential fits to the data (mean constant values ± SE). The number of patches analyzed to compute the mean k_as was WT = 38, K8E = 15, K15E = 14, K20E = 19, K22E = 16, K25E = 15, and K28E = 21; and for k_ds the numbers were WT = 28, K8E = 17, K15E = 16, K20E = 15, K22E = 18, K25E = 14, and K28E = 19. Control WT GsMTx4 constants are shown in black, analogs in gray. (*E*) The calculated effective equilibrium constants (K_D) ± SE are shown. Analogs that were significantly different ($\alpha = 0.05$) from WT are denoted by an *. To see this figure in color, go online.

consistent with control levels of rundown (Fig. S4, *A* and *B*). The potency of each peptide is represented by the percent charge transfer remaining (Fig. 2 *C*) measured at the steady-state level of inhibition during peptide application (Fig. 2 *B*). The summarized results from all patches are shown in Fig. S4 *C*. The WT peptide reduced Piezo1-mediated charge transfer to 38% of its initial levels (Fig. 2 *C*). K8E and K28E had the same potency as WT. However, four analogs (K15E, K20E, K22E, and K25E) inhibited Piezo1 less than the WT showing that the effect was not one of net peptide charge, but of the location of the charges. These four analogs reduced Piezo1 charge transfer by a similar amount (to 55–60% of initial levels), suggesting that these lysines share some functional similarity in inhibition.

To determine if differences in the binding kinetics underlie the losses in activities of the analogs, we calculated effective equilibrium dissociation constants (K_D) from the charge transfer decay and recovery rates as determined with either a double or single exponential model, respectively (Fig. 2, *B*, *D*, and *E*; see Materials and Methods). The K_D for the WT peptide determined by this method (2.0 ± 0.6 μM) was in good agreement with the K_D (2.0 ± 0.2 μM) calculated from a Hill equation fit to the concentration dependence of inhibition of Piezo1 (Fig. S6). The k_a values for the analogs were generally similar to WT, with the exception of K15E, which was significantly greater (shorter time constant). Three of the analogs had k_d values significantly greater than WT (longer unbinding time constants), though there was no strong correlation between this rate constant and compromised inhibition. Further, weaker K_D values were not correlated with the compromised analogs suggesting additional steps in the interaction kinetics that were not revealed in this analysis. It should be noted that the Hill fit from the concentration dependence curve in Fig. S6 predicts a Hill coefficient of 1.5 ± 0.2 suggesting some level of cooperativity. These data suggest that K_D represents more than a typical two-state (free/bound) binding reaction.

The generality of GsMTx4 effects on MSCs was determined by testing it on K^+ selective TREK1 channels expressed in HEK cells. Instead of inhibition, we observed that these channels were potentiated by extracellular GsMTx4 (Fig S7). This suggests that GsMTx4 inhibitory activity is not common to all MSCs probably due to different channel gating mechanisms. Since it was difficult to evaluate the kinetics of potentiation due to the slow washout times and TREK channels being active in resting patches, the analogs were not tested on these channels.

Inhibition of Piezo1 is not influenced by peptide aggregation

Differences in peptide aggregation are another factor that could affect inhibition by modulating the effective concentration of the peptides. The peptides showed different degrees of aggregation, which were especially prevalent at higher concentrations (Fig. S2). Some analogs appear to form larger aggregate sizes than the WT (Figs. S2 and S3), although aggregation appeared to decrease substantially at concentrations used in the Piezo1 experiments (Fig. S3). In addition, the K28E analog, that has a potency equivalent to WT, showed similar aggregation properties to the compromised analog K15E (Fig. S3). These data suggest that, in general, larger multimeric peptide aggregates do not play a significant role in the kinetics or magnitude of Piezo1 inhibition.

Peptide-lipid affinity

To isolate the peptide-lipid binding kinetics from the more complicated channel inhibition kinetics we performed two different lipid vesicle binding assays. The first method determined the binding energy of the peptides to POPG:POPC vesicles by ITC. The resulting isotherms were fitted with a two-site binding model. The fitted isotherms and their corresponding parameters for WT and five of the analogs are shown in Fig. 3 and Table S1. The interactions of the peptides with POPG-POPC liposomes were always exothermic, with the exception of some low-amplitude events at the end of titration for K15E and K28E. In most cases, the smaller of the two binding constants was between 8×10^4 and $8 \times 10^5\ M^{-1}$ (Table S1), corresponding to interaction energies (ΔG) of -28 to -32 kJ/mol. However, curve-fitting identified the presence of a second higher affinity site(s) with constants in the range of 2×10^6 to $3 \times 10^7\ M^{-1}$ of comparable density, as shown by N_1 and N_2. The tight ranges for the negative enthalpies (-0.9 to -1.5 kcal/mol) and positive entropies (20–30 kcal/molK) suggest similarities in the chemistries of binding to both types of sites. K15E had significantly higher binding constants ($8.6 \times 10^6\ M^{-1}$ or -40 kJ/mol), a result that is consistent with the stronger association constant calculated from the inhibition data. It also had a positive ΔH_1 and high ΔS_1, meaning that the low-affinity binding mode is quite different for this analog. K25E had the highest affinity for the second site. The positive entropies probably signify disordering associated with partial desolvation. These experiments do not preclude a larger variety of sites, especially as we recall that the binding site is not chiral specific; however, the model with two sites is sufficient to fit the data.

We also measured the free energy (ΔG) of peptide partitioning into bilayers by following the equilibrium quenching of the intrinsic tryptophan (Trp) fluorescence with titration by lipid vesicles in the presence of the aqueous quenching agent KI (11,33) (Fig. S8). The fluorescence intensity of WT GsMTx4 peaked at 365 nm in solution. This emission peak did not change when bound to lipids (Fig. S8 *A*; Table S2), even though I_{max} for lipid binding showed a robust association (Fig. S8 *B*). The K-E analogs all showed a peak emission intensity that was blue-shifted ~8 nm from WT in solution. This suggests a common effect of net charge on the Trp environment (Fig. S8 *A*), possibly due to differences in analog aggregation (Figs. S2 and S3) increasing shielding of Trp from the aqueous quencher. The K-E analogs also displayed robust association with lipid vesicles (Fig. S8 *B*), although, unlike WT, they were further blue-shifted upon binding (Fig. S8 *A*). This suggests the Trp residues in the analogs were exposed to a more hydrophobic environment, such as deeper membrane penetration than WT (see below).

To determine the affinity of the different peptides to lipids, we fit the vesicle titration curves with a two-state model (adequacy of model is explained in Materials and Methods) and calculated the binding energies from the fluorescence changes (Fig. S8 *B*; Table S2). As shown previously (11), the binding energy of the WT D and L enantiomers to LUVs is only weakly sensitive to the head group charge (Table S2; Fig. S8 *A*). The analogs showed a similar lack of sensitivity to lipid headgroup charge, and the corresponding interaction energies with either type of vesicle (27–34 kJ/mol) were consistent with the ITC data. The differences in interaction energies between WT and the analogs were small for the Trp quenching data. This was similar to the ITC data and patch association rates, supporting the idea that membrane binding differences do not significantly contribute differences in inhibition potency. The second higher affinity sites observed in ITC were not seen in the spectroscopic analysis.

Peptide penetration depth in LUV membranes

To determine the membrane penetration depth we measured Trp fluorescence quenching using vesicles containing brominated lipids. The bromine atoms were located at different positions on the aliphatic chains between carbons 6-7, 9-10, and 11-12, which were 11, 8, and 6 Å from the bilayer center, respectively. We compared WT GsMTx4 with the K25E and K28E analogs that had compromised and uncompromised activity respectively. Quenching was measured in the presence of either 100% BrPC (zwitterionic) or 50:50% POPG:BrPC (anionic) LUVs (Fig. 4, *A* and *B*, respectively). Shallower brominated lipids quenched tryptophan fluorescence better for all peptides, i.e., quenching at C6-7 > C9-10 > C11-12 (Fig. 4 *A* (100% BrPC) and

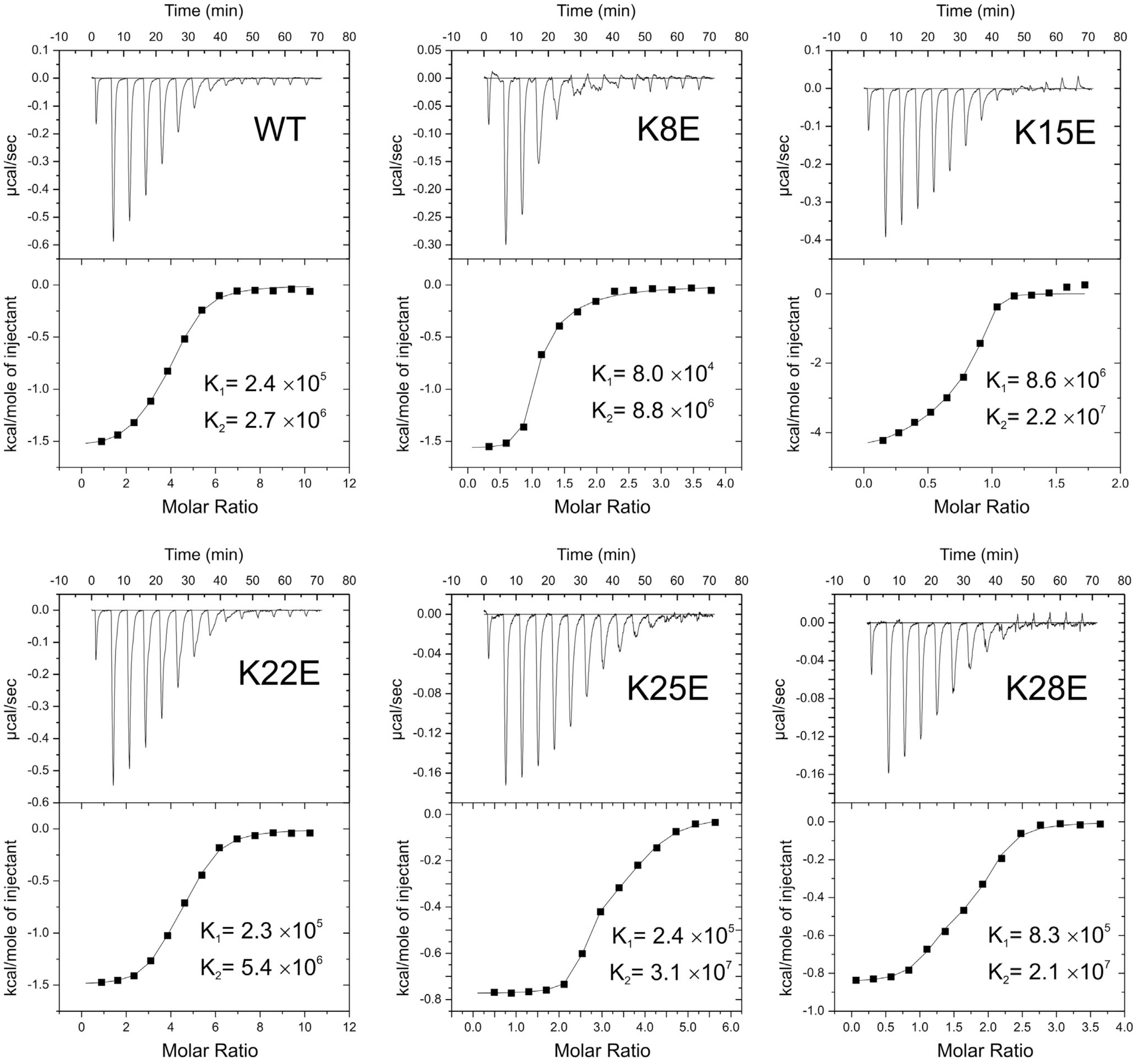

FIGURE 3 Titration isotherms for WT and K-E analogs with different inhibitory capacity suggesting more than one type of binding site in the vesicles. All titrations were done at 30°C with unilamellar POPG:POPC liposomes ($n = 3$). The peptide was present in the chamber at 20–30 μM and liposomes (0.5–1 mM of lipid) were injected (20 μl per step) from a syringe at 300 s intervals.

B (50:50% POPG:BrPC)). These results suggest GsMTx4 WT and the analogs occupy relatively shallow positions in membranes compared with other peptides ((20,46) and see Discussion). However, because of the shallow depth, no peak in the data was observed for the available brominated lipids. So the data were approximated with a Gaussian fit using a priori constraints based on previous experience with other peptides (see Materials and Methods). Although not significantly different, in anionic membranes, the analogs tended to penetrate deeper than WT.

A second method to assess peptide membrane penetration depth used the Trp fluorescence ratio of the peptides in the presence of aqueous (acrylamide) and membrane resident (10-DN) quenching agents (Fig. S9; Table S3). Although greater aggregation of the analogs tended to exaggerate the estimated depth differences, the calculated Stern-Volmer constants suggest that, in general, the K-E analogs bind deeper than the WT.

Surface pressure-dependent monolayer association

Because GsMTx4 modulates the gating of channels that are sensitive to membrane tension, we characterized membrane

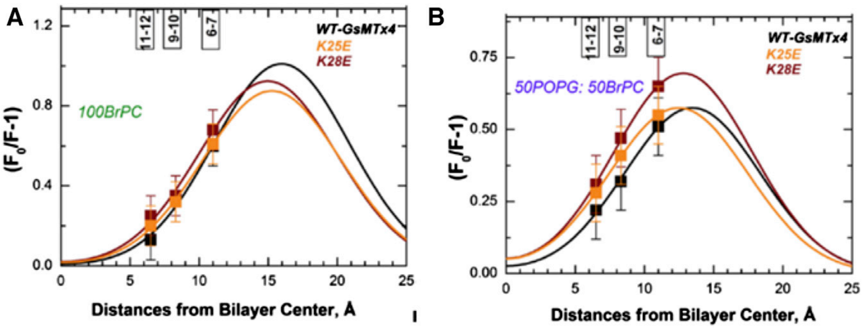

FIGURE 4 Distribution analysis of the depth-dependent fluorescence quenching profiles obtained for WT, K25E, and K28E GsMTx4 in bromolipid containing vesicles. Three bromo PC lipids (brominated at position 6-7, 9-10, and 11-12) were incorporated into LUVs. The quench ratio for the three peptides was plotted with respect to the bromolipid present for both 100BrPC (*A*) and 50POPG:50BrPC (*B*). Data were fitted with a Gaussian function (σ was fixed at 5.0 Å). In the presence of 100BrPC LUV, the Gaussian parameters were $h_m = 16.0 \pm 2.1$ Å, s = 1.0 ± 0.1 for WT-GsMTx4; $h_m = 15.2 \pm 0.4$ Å, s = 0.9 ± 0.1 for K25E; and $h_m = 14.6 \pm 0.9$ Å, s = 0.9 ± 0.2 for K28E. In the presence of 50POPG:50BrPC LUV, the Gaussian parameters were $h_m = 14.0 \pm 0.7$ Å, s = 0.6 ± 0.1 for WT-GsMTx4; $h_m = 12.4 \pm 0.1$ Å, s = 0.6 ± 0.1 for K25E; and $h_m = 12.7 \pm 0.5$ Å, s = 0.7 ± 0.1 for K28E. (h_m indicates the most probable location of the probe (here tryptophan) and s is proportional to quenchibility). All peptide tests have $n = 3$. To see this figure in color, go online.

binding as a function of lipid packing density in a Langmuir trough. The control pressure-area (π-A) isotherms (Fig. 5, *green line*) showed no inflections, and rose smoothly with compression until the monolayer collapsed at ~44 mN/m. The control curve passed 40 mN/m at a molecular area of 68 Å^2, which corresponds to the lipid density in pure POPC bilayers (68.3 Å^2) (47). The surface pressure that packs lipids at this bilayer density is called the monolayer-bilayer equivalence pressure (πB). For many lipids πB is traditionally defined in the range of 30–35 mN/m (48), but according to Brockman (49) the πB for a similar SOPC lipid is near 40.5 mN/m, which is closer to the collapse pressure observed here.

Addition of 0.1 μM WT peptide into the subphase visibly increased surface pressure over a wide range of areas. At 1 μM or above, GsMTx4 increased surface pressure immediately, i.e., without compression, signifying massive intercalation into the monolayer at low packing density. As seen from the family of curves (Fig. 5), the increase in surface pressure is concentration-dependent. Up to ~37 mN/m, the compression curves lay above the control. However, above that pressure the GsMTx4 curves bent and intersected with the control. The bend could be due to repartitioning of the peptide from the film into the subphase or due to the peptide moving from a deeper penetration depth to the surface. The peptide pressure curves intersect the control curve in the vicinity of 40 mN/m, i.e., near πB. The flattening of the curves at this level probably marks the expulsion of the peptide that continues during a gradual collapse of the monolayer. The area, at which the transition (the break point) occurred, increased with peptide concentration, while the pressure at the bending point decreased. The untreated monolayer seems to withstand higher pressure before collapsing than it can in the presence of peptide. The shape of the curve gets more complicated at 3 μM, so we focused on 1 μM where an inflection occurred but the curves maintained a similar shape.

The bending of the isotherm near the monolayer-bilayer equivalence pressure (Fig. 5, arrows) suggests that the peptide-harboring film undergoes a phase transition. This is better illustrated in Fig. 6 *A*, in which the control monolayer (no peptide) π-A isotherm (*top*) and the corresponding inverse compressibility Cs^{-1} plot (*bottom*), representing stiffness of the film, are compared with the traces measured in the presence of WT GsMTx4. The monolayer stiffness in peptide-free controls shows a monotonic growth with compression, reaching a maximum of ~80 mN/m in the vicinity of monolayer-bilayer equivalence pressure (πB), followed by a sharp decrease signifying collapse. In contrast, the stiffness of the film in the presence of GsMTx4 exhibits several minima. The first reproducible minimum observed between 110 and 130 Å^2 coincides with inflection in the middle of the isotherm at π~25–30 mN/m. This inflection may reflect some compaction, reorientation, or ordering of the peptide in the film. The second minimum observed toward the end of compression (near 80 Å^2 per molecule) most likely reflects a shift of the peptide from a deeper to a shallower position in the monolayer or to a peripherally absorbed state. This reversible partitioning of the peptide between the surface (see Discussion) and deeper positions suggests that, near the πB, changes in the area will not change lateral pressure/tension significantly, producing a pressure (or tension) clamp effect.

We compared the π-A and Cs^{-1} isotherms of WT with four analogs having inhibitory activities that were either reduced (K15E and K25E) or unchanged (K8E and K28E) compared with WT (Fig. 6, *B–E*). The value of ${Cs_1}^{-1}$ corresponding to the first minimum (Table 1) is reproducibly higher for WT GsMTx4 than for other analogs suggesting that the peptide resides in a more stable conformation in the expanded monolayer. The compression isotherms for the WT and the analogs with WT level of activity intersect with the control curves near πB and the rigidity curves (Cs^{-1}) show clear second minimums of 13–14 mN/m in that region (see regions marked with asterisk in Fig. 6, *B–E*, and Table 1). For the compromised K15E, the second Cs^{-1} minimum was considerably higher (~22 mN/m), whereas for K25E it was completely absent, though Cs^{-1} was clearly above ~25 mN/m in this region. This behavior shows that the peptide residence in the lipid film in this region is strongly dependent on lateral pressure. WT peptide tends to "clamp" the tension near the

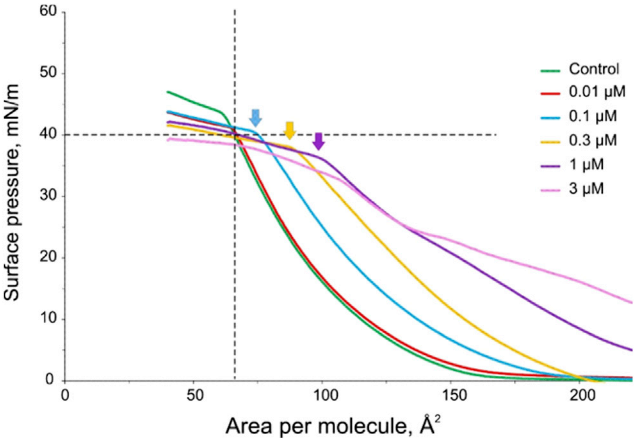

FIGURE 5 Representative pressure-area isotherms taken with different concentrations of WT GsMTx4 in the subphase. Qualitatively similar interactions of WT GsMTx4 with POPG-POPC monolayers at different concentrations are illustrated by compression isotherms. Visible monolayer "swelling" is observed at subphase peptide concentrations of 0.1 μM and above. The peptide tightly binds to the expanded monolayer. There is no obvious effect of gradual "squeezing-out" of the peptide from the monolayer at higher pressures. The monolayer instead has a tendency to collapse earlier (*arrows*) as the peptide concentration increases and pressure approaches 37–40 mN/m. In the control, the monolayer collapsed at 43–45 mN/m. The statistics are presented in Table 1. To see this figure in color, go online.

monolayer-bilayer equivalence pressure. K8E and K28E, which have uncompromised activity, resemble the WT isotherm in that region. In contrast, the partially active peptides K15E and K25E exhibited a different behavior near πB (Fig. 6). Their π-A curves lay above and do not intersect with the control curve. The Cs_1^{-1} parameter does not show a minimum, rather a local maximum (asterisk). This indicates that the peptides have greater stability in the lipid film near πB and never completely leave it. Based on the compression isotherms, the K15E and K25E analogs will not be able to clamp the pressure (tension) in the peptide exposed monolayer as effectively as WT.

To visualize the area occupied by the peptide we replotted the pressure-area curves in area-pressure coordinates and presented the area difference in log scale (Fig. S10). This shows that the logarithmic slope of the monolayer area decrease with pressure reflects the molecular area (a) of the expelled peptide. For WT GsMTx4, a is estimated as 3.3 nm^2 per molecule, whereas for the compromised K25E a is only 0.87 nm^2. The reduction of inhibitory activity in different analogs correlates with stable residence of peptides in the monolayer.

Modeling WT peptide association with monolayers supports tension-dependent depth changes

We visualized monolayer-peptide interactions by performing atomistic MD simulations in a peptide-containing POPC monolayer/water/vacuum system. The monolayer surface tension was varied over the range corresponding to effective membrane pressures (π_{eff}) between 0 and 100 mN/m (as described in Materials and Methods). The monolayer was laterally compressed at the $\pi_{eff} = 100$ mN/m and expanded and reached a rather disordered state at the $\pi_{eff} = 0$ as expected (Fig. 7, *A* and *B*). In the area/lipid versus pressure plot (Fig. 7 *C*), we see that the area/lipid is greater over the entire range of pressures when peptide is present, consistent with the experimental results shown in Fig. 6. Also, in agreement with the experimental data, the area/lipid difference between pure lipid and peptide containing monolayers decreases as pressure increases (7 Å^2 at 0 mN/m vs. 3.5 Å^2 at 100 mN/m) representing peptide expulsion and a corresponding loss of peptide area contribution. K15E produced a nearly identical π_{eff}-area curve to that of the WT-containing monolayer. This is more clearly illustrated when we plot the relation between pressure generated changes in lipid area and peptide depth (Fig. 7 *D*). WT was located at shallow positions relative to the POPC phosphorus atoms in condensed monolayers (areas/lipid of 54–60 Å^2) under high pressures and moved to lower (deeper) positions in expanded monolayers (areas/lipid of 65–85 Å^2) at low pressures. Analysis of acyl chains atoms that were in contact with WT supported these results; at high π_{eff}, the acyl chain atoms in contact with WT exhibited a skewed pattern, that is, there were far more frequent contacts of shallowly positioned atoms (i.e., C2 and C3) relative to C16–C18 atoms. In contrast, at low π_{eff} the pattern was less skewed. (Fig. S11). Although not statistically significant we observed a trend for K15E to remain deeper than WT peptide at high pressures (data not shown). Longer simulation times would likely produce results more closely aligned with the experimental data. Although the simulated pressure-area curves and corresponding depth changes do not precisely duplicate the experimental data, the results support the general mechanism and qualitatively illustrate the trend for peptide relocation between the deep and shallow positions depending on pressure.

DISCUSSION

GsMTx4 tension-clamping model

The previous model of GsMTx4 inhibition of MSCs (1) postulated that static association of the peptide with a relaxed bilayer distorted the local membrane thickness/curvature near the channel so that greater membrane tension would be required to induce channel gating. However, MD simulations predict that GsMTx4 and other ICK peptides produce only minor local membrane perturbations (25,29,30). We showed that in relaxed membranes GsMTx4 is most stable in a shallow, surface-absorbed mode (Fig. 7) (29,30). When the bilayer is stretched the lateral pressure decreases (17,50) and GsMTx4 sinks deeper, acting as a local tension/area clamp. Our model suggests that residue

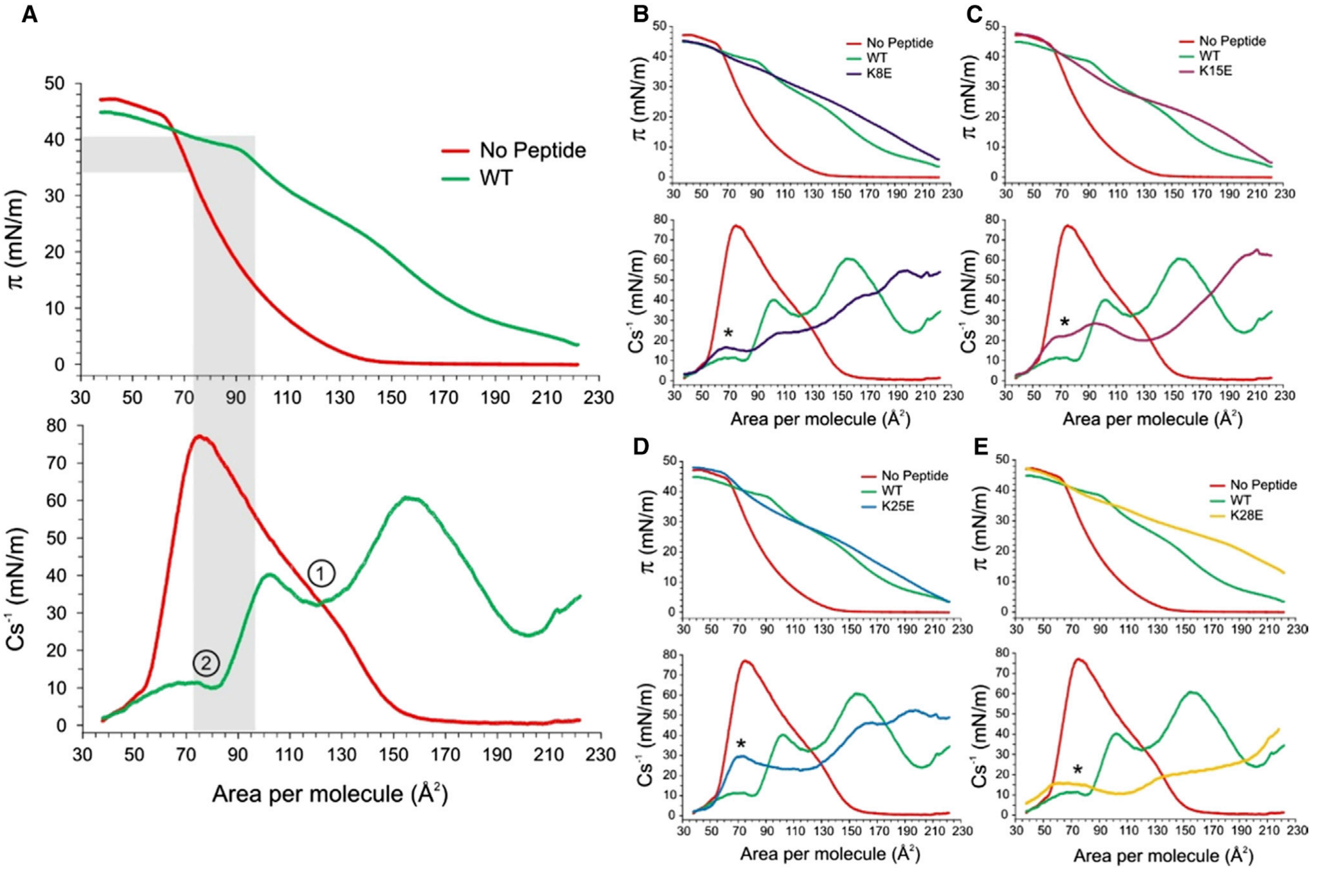

FIGURE 6 Compression (*π-A*) and inverse compressibility modulus ($Cs^{-1} = A \times (d\pi/dA)$) isotherms of POPG-POPC monolayers in the presence of 1 μM WT GsMTx4 (*A*), K8E (*B*), K15E (*C*), K25E (*D*), and K28E (*E*). WT (*green*) and control (*red*) curves are repeated on (*B–E*) for comparison. The control monolayers, only lipids, compress smoothly with no phase transition. The monolayer collapses near 41.7 ± 2.9 mN/m ($n = 3$). At the πB taken as 40 mN/m (48), the molecular area per lipid is 66 ± 2.9 Å^2. Plots of Cs^{-1} that reflect stiffness of the monolayer are aligned on the area scale with the compression isotherms. For WT GsMTx4 (*A*), the Cs^{-1} plot exhibits two characteristic minima (designated *1* and *2*). The first minim takes place in the middle of the compression isotherm, whereas the second minimum reached at 60–80 Å^2/molecule occurs near the monolayer-bilayer equivalence pressure (πB). The gray shading highlights the area and pressure ranges where the presence of GsMTx4 may exert physiological effects. All analogs with normal activity exhibit low Cs^{-1} values in that region indicating a facilitated pressure-dependent exchange of the peptide between "deep" and "superficial" states in the film. In the areas marked by the asterisk (*B–E*), the isotherms for the less-active peptides (K15E and K25E) are elevated higher above the control monolayer curves than K8E and K28E. Instead of a second minimum or low plateau as in WT (*green curves*), an additional peak in Cs^{-1} is present for K15E and K25E indicating higher stiffness and no exchange. These traits suggest tighter association of the less-active peptides with the lipid; their position in the film is not as strongly perturbed by pressure. To see this figure in color, go online.

changes that shift the binding equilibrium toward deeper penetration in relaxed membranes could lower the efficacy of the peptide as an area buffer when tension increases. Our findings reconcile well with other recent studies on the mechanism of inhibition of peptide toxins (23,24) and atomistic simulations of GsMTx4 and the K-E analogs (41).

Effects on MSC gating

Eukaryotic MSCs fall into two categories: 1) Piezo- and TRP channels that cause depolarization and 2) the K$^+$-selective channels of the 2P domain family that are hyperpolarizing. The crystal structure of 2P domain channels supports a model with the channel mechanosensory elements located on the cytoplasmic leaflet of the membrane (51). Recent cryoelectron microscopic structural data for the Piezo1 channels tentatively place the mechanosensory structures on the outer leaflet (52). Thus, it would be predicted that tension-dependent depth changes of GsMTx4 in the outer leaflet would have different effects on Piezo and 2P domain channels. Our data support this assertion as the external application of GsMTx4 inhibits Piezo but potentiates TREK-1 channels. This property occurs because the inner monolayer is coupled to the outer monolayer (53) due to interdigitation of acyl chains (50) so that tension changes in one monolayer are transferred to the other leaflet. Thus the GsMTx4 mediated area expansion of the outer leaflet could transfer tension to the fixed-area inner monolayer resulting in TREK potentiation. The mechanosensitive bacterial channels MscL and MscS are also sensitive to GsMTx4 in a concentration-dependent manner, showing inhibition at low concentrations and potentiation at high concentration

TABLE 1 Mechanical Parameters of 75POPG:25POPC Monolayers in the Presence of 1 μM of GsMTx4 and Several K-E Analogs

	Breaking Point		2nd Minimum		1st Minimum		
Analog	A (Å^2)	π (mN/m)	Cs^{-1} (mN/m)	π (mN/m)	Cs^{-1} (mN/m)	π (mN/m)	n
Control	66.0 ± 2.9	41.7 ± 2.9	–	–	–	–	9
WT	89.8 ± 4.1	38.7 ± 0.9	14.3 ± 2.6	39.5 ± 0.5	32.2 ± 4.0	26.1 ± 1.5	10
K8E	51.7 ± 3.2	43.7 ± 0.9	13.7 ± 2.3	36.9 ± 0.9	21.3 ± 2.2	30.8 ± 1.1	8
K15E	52.3 ± 2.2	43.7 ± 0.2	21.8 ± 1.2	40.5 ± 0.6	19.7 ± 1.0	26.4 ± 0.3	4
K25E	59.8 ± 1.8	47.1 ± 0.6	–	–	22.2 ± 1.5	29.3 ± 1.7	8
K28E	56.7 ± 7.2	43.8 ± 1.4	13.3 ± 2.5	35.5 ± 1.0	20.5 ± 1.4	28.8 ± 0.7	4

Breaking point of isotherms signifies the change of slope, which in case of WT shows the early onset of peptide expulsion. For all other analogs an obvious isotherm flattening was associated with collapse. The position of the second minimum of the inverse compressibility parameter $Cs_2{}^{-1}$ reflects "softening" of the monolayer associated with pressure-dependent redistribution of the peptide to a shallower position. The second minima are low for the active peptides, but are either higher for the compromised peptides (K15E), or may not even exist (K25E). The first $Cs_1{}^{-1}$ minimum presumably reflects compaction and ordering of the peptides within the still expanded monolayer and its position shows no direct correlation with activity. The number of experiments is shown in the last column (n).

(54). But these channels likely have a different gating mechanism from eukaryotic channels based on their sensitivity to membrane thickness (55,56) and relatively high activation tensions (MscL and MscS require 7–14 mN/m half activation compared with 3–4 mN/m for Piezo).

The role of lysines in peptide binding

Lysine plays a key role in stabilizing proteins at the membrane interface (21,22) through energetically favorable interactions with carbonyl and phosphate groups at the bilayer interface. The six lysines on GsMTx4 cover most of the hydrophilic surface and stabilize the shallow binding mode. Simulations also reveal a deep-binding mode where lysines 15, 20, 22, and 25 stabilize the peptide at the water-bilayer interface (25,41), whereas lysines 8 and 28 interact with the opposing monolayer surface. All analogs with changes to lysines that stabilize the interaction with the outer leaflet (K15E, K20E, K22E, and K25E) showed a similar reduction in potency, suggesting equivalent roles. However, K8E and K28E analogs have uncompromised activity against Piezo1 supporting the model where amino acids that promote deeper insertion will reduce redistribution of the peptide under lateral tension and diminish its effectiveness as an "area reservoir."

GsMTx4 association with relaxed membranes is strong and shallow, but channel inhibition is not simply a function of lipid binding strength

The energy of binding to lipids was largely unaffected by the K-E analogs revealing an independence from net charge. This supports our previous analysis showing that peptide-lipid dynamics do not reflect total charge and that GsMTx4's *effective charge* (Z_{eff}) is low as estimated from the slope of ΔG versus surface potential (11). This weak contribution of charge to binding suggests that association is dominated by the positive entropic energy (*energy change is negative*) caused by desolvation. The negative ΔG of desolvating the hydrophobic face is relatively large compared with the electrostatic repulsion from the positive charge of the methylamines on POPC.

Estimates of binding energies for the peptides to POPG:POPC vesicles were in close agreement, primarily between 27–34 kJ/mol by both the tryptophan fluorescence quenching and ITC assays. These differences in binding energies were relatively small and there was no correlation between lower binding energies and decreased Piezo inhibition potency. This implies a more complicated process than a simple two-state binding reaction as we concluded from the effective equilibrium constants derived from the inhibition kinetics. This was also suggested by the presence of at least two binding sites for all peptides in the ITC isotherms. The first constant may represent the binding energy of monomers and/or multimers into the shallow position, whereas the second higher affinity site may represent a deeper bound mode, or the energy for dissolution of multimers (see below). The π-A isotherms from the monolayer experiments also suggest the existence of different binding modes. Absorption to the surface and subsequent deeper penetration has been seen for antimicrobial, viral, and signaling peptide binding (57), though the tension dependence of this property has never been tested. Other factors such as absorption versus partitioning, lateral diffusion to the channel and interaction with specific lipids may also contribute to the observance of multimode binding kinetics.

The binding energies to zwitterionic POPC membranes as measured by Trp quenching (25–26 kJ/mol), were in good agreement with the predicted binding energies from our companion MD study (18–27 kJ/mol) in the same lipid environment (41). These simulations suggest that GsMTx4 stably resides at the shallow binding depths compared with Hanatoxin (58) and HpTx2 (29). This is supported by the brominated lipids quenching experiments placing both WT and analog peptides at a shallow depth (>12 Å from the bilayer center) compared with toxins that interact with voltage-gated channel intramembrane gates like SGTx (9 Å (20)) and Hanatoxin (8 Å (46)). Both the brominated lipids and acrylamide/10-DN Trp quenching experiments suggest the K-E analogs penetrate deeper than WT in

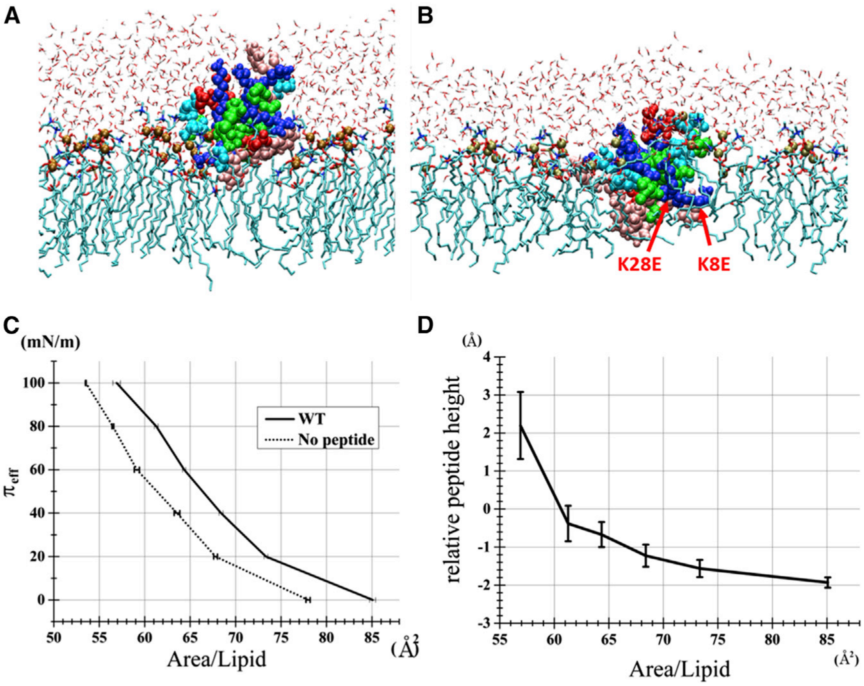

FIGURE 7 Representative structures of the POPC monolayer simulations. (*A*) A snapshot from a trajectory with the π_{eff} of 100 mN/m (i.e., surface tension coupled to -10 mN/m). WT atoms are shown as Van der Waals spheres with the amino acid (*single letter designation*) residues colored in pink (W, F), green (A, C, L, P), blue (R, K), cyan (S, T, N, G), and red (D, E). POPC phosphorus atoms are highlighted in large ocher spheres. Other atoms/groups are presented as follows: lime licorice (POPC acyl chains), cyan, red, and blue licorice (carbon, oxygen, and nitrogen atoms of POPC headgroup), and thin licorice (water molecules). (*B*) A snapshot from the simulations with $\pi_{eff} = 0$ mN/m (i.e., surface tension coupled to 90 mN/m), with the same representation scheme as in (*A*). The two lysines that when changed to glutamates produced uncompromised analogs are indicated showing greater depth under higher tension. (*C*) The relationship between the π_{eff} and the membrane area in the WT-containing (and control) POPC monolayer simulations. Vertical axis shows the π_{eff} derived from the monolayer surface tension as described in Materials and Methods. The horizontal axis shows the total area of the POPC monolayer of the simulation box after simply being divided by the number of the POPC molecules (i.e., 40). The mean ± SE of the 20 trajectories that were subjected to the stepwise compression/expansions are plotted. (*D*) Position along the membrane normal (penetration depth) of the WT peptide as a function of the membrane area. Horizontal axis shows the total area of the POPC monolayer of the simulation box simply divided by the number of the POPC molecules (i.e., 40). Vertical axis shows the height of WT center of mass relative to the mean *z*-coordinate of phosphorus atoms of POPC calculated as described in Materials and Methods. The mean ± SE of the 20 trajectories are plotted. To see this figure in color, go online.

relaxed bilayers. However, K28E that had WT levels of inhibitory efficacy also showed deeper penetration. This may be due to the assays' insensitivity to differences between changes in the peptide center of mass versus tilt. Both the tilt of the peptides with respect to the plane of the bilayer surface, and overall peptide binding depth, can influence Trp fluorescence and the surface area occupied by the peptide in a relaxed membrane. In simulations of the K-E peptides in bilayers, many of the analogs displayed significant (1–2 Å) tilt of the Trp residues compared with WT (41).

Tension-dependent insertion

As expected for amphipaths, GsMTx4 and its analogs showed strong partitioning into the water-air interface. As the monolayer approaches the bilayer equivalence pressure (25–37 mN/m) the WT isotherm transitions to a shallow compression slope corresponding to the first dip in compressibility, likely reflecting changes in tilt or depth of the peptides as they are compacted by the lipids (Fig. 6 *A*, *top panel*). Upon reducing the surface area further, the slope of the pressure increase becomes even shallower through πB and up to the point of collapse. This strongly contrasts with the progressive increase in pressure in control monolayers. We suspect this represents a massive expulsion of peptide at compressions approaching the monolayer-bilayer equivalence pressure (πB ~37–40 mN/m). The structure of GsMTx4 (59) has dimensions of ~2 × 2 nm, predicting that the maximal area that can be occupied by the peptide in the plane of the membrane is ~4 nm^2. The steep slope transition in the WT compression curve (Cs^{-1}) predicts expulsion of peptides occupying an effective area of 3.3 nm^2 at a depth of ~1.5 nm, just below πB. At 1 μM, this would represent the bulk of the peptide's "area reservoir." Thus, at πB the peptide would protrude and occupy less area giving it greater area buffering capacity. When tension is applied to a bilayer as in a patch, that tension is predominately in the outer monolayer that is constrained by the patch electrode surface (60,61). External application of GsMTx4 allows for expansion of the outer monolayer with respect to the inner monolayer. Due to the coupling of the outer to the inner monolayer (53), the inner monolayer now takes a larger share of the total tension, so tension in the *outer monolayer* is reduced and Piezo gating inhibited.

All analogs had modified π-A isotherms compared with WT. However, the two compromised analogs (K15E and K25E) have significantly lower compressibility near πB and less than half the area change of WT (Fig. S10). The two uncompromised analogs, K8E and K28E, had area changes comparable with WT and the MD simulations predicted these lysines stabilize the deep binding mode (41).

Increasing bilayer surface tension in the simulations (varied between 60 and 75 mN/m) causes the WT peptide to sink deeper into the membrane by ~1Å (41). In contrast, peptide/monolayer simulations showed the peptide sinking deeper when the area/lipid ratio is near πB. We also observed that higher pressures (~100 mN/m for an area change from 57 to 85 Å^2) are required in simulations than under experimental conditions (~10mN/m) (Fig. 5). The analysis of expulsion areas has also suggested possible peptide dimerization (see dimensional changes predicted from the slope of the area-pressure plot in Fig. S10 and (41)), increasing the area buffering capacity.

The incremental cross-sectional areas may represent the expulsion of peptides, perhaps including peptides leaving the membrane with lipids attached. From the pressure midpoint of the last transition for WT (π = 40 mN/m), we estimate the energy of insertion ΔG = area $\times$ π = -79 kJ/mol, which translates into a very high affinity with $K_D = 6.9 \times 10^{13}$ M^{-1}. Thus, the estimated insertion energy must be steeply dependent on the lipid area displaced by the peptide. If we reduce the area by half ($a = 1.65$ nm^2), then the insertion energy drops to $\Delta G = -39$ kJ/mol, giving $K_D = 8 \times 10^6$ M^{-1}, which is much closer to the measured affinities. From this calculation we might infer that the peptides are expelled as dimers (see below) or with clusters of lipids. If the process of expulsion is concomitant with collapse, then the peptide may induce nonlamellar structures that are in equilibrium with the lamellar part, precisely at πB. This would create another peptide/lipid buffer that could "clamp" the tension in the monolayer.

Effects of aggregation on membrane-binding kinetics are minimal

Dynamic light scattering (DLS) showed that, in most cases, the reduced charge on the analogs increased aggregation, which may affect bilayer interactions and the effective peptide concentration. However, K15E (compromised) and K28E (uncompromised) show similar levels of aggregation as concentration decreases. It is also possible that aggregation is responsible for the appearance of the additional negative peak at 225–230 nm in CD spectra of analogs in solution. Aggregation can effect exciton splitting produced by B_b transition in tryptophan absorbance (62), which is known to affect CD spectra in peptides containing several Trp residues (63). Whatever the cause, this feature disappears upon binding to POPC:POPG LUV, indicating that there is no substantial difference in the fold of the WT and mutant peptides.

Although larger aggregate structures do not appear to affect analog activity, smaller multimeric assemblies may play a role in inhibition. Our MD study shows that dimers sometimes form when associated with the membrane that was stable for more than 300 ns, with one peptide inserted in the bilayer and the second peptide riding on top of the first (41). When tension was applied to the bilayer, the second stacked peptide rotates to partition into the bilayer. Experimental and MD simulations of antimicrobial cationic peptides show a similar mechanism of binding where peptide dimers are attracted to the membrane surface, followed by sinking of the hydrophobic cores into the bilayer (64). This might explain the Hill coefficient of 1.5 observed for the concentration dependence of inhibition. Thus, an alternative to the monomer-depth change model is partitioning of surface-absorbed multimers into the bilayer as tension changes.

CONCLUSIONS

The bilayer lateral pressure/tension profile, when altered by membrane stretching, works on MSCs, favoring states with larger in-plane areas (65–69). The data suggest that GsMTx4, acting as a "mobile reserve" of membrane material, incorporates into the membrane in a tension-dependent manner and distorts the distribution of tension near the channel, making the transfer of force from the bilayer to the channel less efficient. This is fully consistent with the earlier observation that GsMTx4 does not block the pore, but produces a rightward shift of the tension-activation curve (3). GsMTx4 primarily resides in a shallow mode that is in a tension-dependent equilibrium between a surface-adsorbed state (low surface area) and deeper insertion as the free volume increases (17). Changes to lysine residues that surround the hydrophobic face of the peptide and stabilize the shallow mode allow the peptide to penetrate deeper and possibly tilt in the relaxed membrane, reducing the peptide's area reservoir and shifting lateral pressure that drives the partitioning between the shallow and deep states. The tension-dependent depth changes of GsMTx4 modulate the area of the outer monolayer inhibiting Piezo activation. These same principles likely apply to other amphipathic molecules (70). Although all amphipaths affect monolayer area, the magnitude of their effect on MSCs depends on the tension at the relevant depths, which appears to be a key difference between GsMTx4 and other ICK peptide inhibitors.

SUPPORTING MATERIAL

Supporting Material and Methods, eleven figures, and three tables are available at http://www.biophysj.org/biophysj/supplemental/S0006-3495(16)31041-4.

AUTHOR CONTRIBUTIONS

R.G.—electrophysiological recordings of Piezo1 and TREK1 channels, testing sensitivity to GsMTx4 and analog peptides, native gel electrophoresis of peptide aggregation, data analysis, interpretation, and drafting and editing the manuscript; C.G.—tryptophan quenching and vesicle protection experiments, binding affinity determination, depth of penetration, CD spectrum of native structures, and editing of manuscript; A.Y.—tension-dependent peptide depth measurements, isothermal calorimetry, dynamic light scattering assessment of aggregation, data analysis, and manuscript editing; K.N.—molecular dynamics simulations, data analysis, and manuscript editing; F.S.—conception and design of the experiments, interpretation of data, and critically revising manuscript; A.S.L.—conception and design of the experiments, analysis and interpretation of data, and drafting and critically revising the manuscript; S.I.S.—conception and design of the experiments, analysis and interpretation of data, and drafting and critically revising the manuscript; and T.M.S.—conception and design of the experiments, analysis and interpretation of data, and drafting and critically revising the manuscript.

ACKNOWLEDGMENTS

This work was funded by a DoD grant, project No. DM102091, NIH grant HL054887 (to F.S.), NIH grant RO1 GM069783 (to A.S.L.), and NIH grant R01 GM107652 (to S.I.S.).

REFERENCES

1. Suchyna, T. M., S. E. Tape, …, P. A. Gottlieb. 2004. Bilayer-dependent inhibition of mechanosensitive channels by neuroactive peptide enantiomers. *Nature.* 430:235–240.
2. Suchyna, T. M., J. H. Johnson, …, F. Sachs. 2000. Identification of a peptide toxin from *Grammostola spatulata* spider venom that blocks cation-selective stretch-activated channels. *J. Gen. Physiol.* 115:583–598.
3. Bae, C., F. Sachs, and P. A. Gottlieb. 2011. The mechanosensitive ion channel Piezo1 is inhibited by the peptide GsMTx4. *Biochemistry.* 50:6295–6300.
4. Shirokova, N., and E. Niggli. 2013. Cardiac phenotype of Duchenne Muscular Dystrophy: insights from cellular studies. *J. Mol. Cell. Cardiol.* 58:217–224.
5. Gailly, P. 2012. TRP channels in normal and dystrophic skeletal muscle. *Curr. Opin. Pharmacol.* 12:326–334.
6. Bagriantsev, S. N., E. O. Gracheva, and P. G. Gallagher. 2014. Piezo proteins: regulators of mechanosensation and other cellular processes. *J. Biol. Chem.* 289:31673–31681.
7. Gu, Y., and C. Gu. 2014. Physiological and pathological functions of mechanosensitive ion channels. *Mol. Neurobiol.* 50:339–347.
8. Hara, M., K. Tabata, …, R. Tatsumi. 2012. Calcium influx through a possible coupling of cation channels impacts skeletal muscle satellite cell activation in response to mechanical stretch. *Am. J. Physiol. Cell Physiol.* 302:C1741–C1750.
9. Norton, R. S., and P. K. Pallaghy. 1998. The cystine knot structure of ion channel toxins and related polypeptides. *Toxicon.* 36:1573–1583.
10. Bosmans, F., and K. J. Swartz. 2010. Targeting voltage sensors in sodium channels with spider toxins. *Trends Pharmacol. Sci.* 31:175–182.
11. Posokhov, Y. O., P. A. Gottlieb, …, A. S. Ladokhin. 2007. Is lipid bilayer binding a common property of inhibitor cysteine knot ion-channel blockers? *Biophys. J.* 93:L20–L22.
12. Lee, S. Y., and R. MacKinnon. 2004. A membrane-access mechanism of ion channel inhibition by voltage sensor toxins from spider venom. *Nature.* 430:232–235.
13. Wang, J. M., S. H. Roh, …, K. J. Swartz. 2004. Molecular surface of tarantula toxins interacting with voltage sensors in K(v) channels. *J. Gen. Physiol.* 123:455–467.
14. Jung, H. J., J. Y. Lee, …, J. I. Kim. 2005. Solution structure and lipid membrane partitioning of VSTx1, an inhibitor of the KvAP potassium channel. *Biochemistry.* 44:6015–6023.
15. Wee, C. L., D. Gavaghan, and M. S. Sansom. 2010. Interactions between a voltage sensor and a toxin via multiscale simulations. *Biophys. J.* 98:1558–1565.
16. Cox, C. D., C. Bae, …, B. Martinac. 2016. Removal of the mechanoprotective influence of the cytoskeleton reveals PIEZO1 is gated by bilayer tension. *Nat. Commun.* 7:10366.
17. Markin, V. S., and F. Sachs. 2015. Free volume in membranes: viscosity or tension? *Open J. Biophys.* 5:80–83.
18. Phillips, R., T. Ursell, …, P. Sens. 2009. Emerging roles for lipids in shaping membrane-protein function. *Nature.* 459:379–385.
19. Ostrow, K. L., A. Mammoser, …, P. A. Gottlieb. 2003. cDNA sequence and in vitro folding of GsMTx4, a specific peptide inhibitor of mechanosensitive channels. *Toxicon.* 42:263–274.
20. Jung, H. H., H. J. Jung, …, J. I. Kim. 2010. Structure and orientation of a voltage-sensor toxin in lipid membranes. *Biophys. J.* 99:638–646.
21. Caputo, G. A., and E. London. 2003. Cumulative effects of amino acid substitutions and hydrophobic mismatch upon the transmembrane stability and conformation of hydrophobic alpha-helices. *Biochemistry.* 42:3275–3285.
22. Killian, J. A., and G. von Heijne. 2000. How proteins adapt to a membrane-water interface. *Trends Biochem. Sci.* 25:429–434.
23. Gupta, K., M. Zamanian, …, K. J. Swartz. 2015. Tarantula toxins use common surfaces for interacting with Kv and ASIC ion channels. *eLife.* 4:e06774.
24. Schmidt, D., and R. MacKinnon. 2008. Voltage-dependent K+ channel gating and voltage sensor toxin sensitivity depend on the mechanical state of the lipid membrane. *Proc. Natl. Acad. Sci. USA.* 105:19276–19281.
25. Nishizawa, M., and K. Nishizawa. 2007. Molecular dynamics simulations of a stretch-activated channel inhibitor GsMTx4 with lipid membranes: two binding modes and effects of lipid structure. *Biophys. J.* 92:4233–4243.
26. Wee, C. L., D. Bemporad, …, M. S. Sansom. 2007. SGTx1, a Kv channel gating-modifier toxin, binds to the interfacial region of lipid bilayers. *Biophys. J.* 92:L07–L09.
27. Wee, C. L., M. B. Ulmschneider, and M. S. P. Sansom. 2010. Membrane/toxin interaction energetics via serial multiscale molecular dynamics simulations. *J. Chem. Theory Comput.* 6:966–976.
28. Bemporad, D., Z. A. Sands, …, M. S. Sansom. 2006. Vstx1, a modifier of Kv channel gating, localizes to the interfacial region of lipid bilayers. *Biochemistry.* 45:11844–11855.
29. Chen, R., and S. H. Chung. 2013. Effect of gating modifier toxins on membrane thickness: implications for toxin effect on gramicidin and mechanosensitive channels. *Toxins (Basel).* 5:456–471.
30. Nishizawa, K. 2011. Atomistic molecular simulation of gating modifier venom peptides—two binding modes and effects of lipid structure. *In* Mechanosensitivity and Mechanotransduction. A. Kamkin and I. Kiseleva, editors. Springer, Tokyo, Japan, pp. 167–190.
31. Suchyna, T. M., V. S. Markin, and F. Sachs. 2009. Biophysics and structure of the patch and the gigaseal. *Biophys. J.* 97:738–747.
32. Motulsky, H. 2013. Intuitive Biostatistics: A Nonmathematical Guide to Statistical Thinking. Oxford University Press, New York.
33. Posokhov, Y. O., P. A. Gottlieb, and A. S. Ladokhin. 2007. Quenching-enhanced fluorescence titration protocol for accurate determination of free energy of membrane binding. *Anal. Biochem.* 362:290–292.
34. Ladokhin, A. S., S. Jayasinghe, and S. H. White. 2000. How to measure and analyze tryptophan fluorescence in membranes properly, and why bother? *Anal. Biochem.* 285:235–245.
35. Ladokhin, A. S. 1999. Analysis of protein and peptide penetration into membranes by depth-dependent fluorescence quenching: theoretical considerations. *Biophys. J.* 76:946–955.
36. Ladokhin, A. S. 2014. Measuring membrane penetration with depth-dependent fluorescence quenching: distribution analysis is coming of age. *Biochim. Biophys. Acta.* 1838:2289–2295.
37. Ladokhin, A. S. 1999. Evaluation of lipid exposure of tryptophan residues in membrane peptides and proteins. *Anal. Biochem.* 276:65–71.
38. Smaby, J. M., M. M. Momsen, …, R. E. Brown. 1997. Phosphatidylcholine acyl unsaturation modulates the decrease in interfacial elasticity induced by cholesterol. *Biophys. J.* 73:1492–1505.

39. Oostenbrink, C., A. Villa, …, W. F. van Gunsteren. 2004. A biomolecular force field based on the free enthalpy of hydration and solvation: the GROMOS force-field parameter sets 53A5 and 53A6. *J. Comput. Chem.* 25:1656–1676.
40. Poger, D., and A. E. Mark. 2010. On the validation of molecular dynamics simulations of saturated and cis-monounsaturated phosphatidylcholine lipid bilayers: a comparison with experiment. *J. Chem. Theory Comput.* 6:325–336.
41. Nishizawa, K., M. Nishizawa, …, T. M. Suchyna. 2015. Effects of Lys to Glu mutations in GsMTx4 on membrane binding, peptide orientation, and self-association propensity, as analyzed by molecular dynamics simulations. *Biochim. Biophys. Acta.* 1848:2767–2778.
42. Kaznessis, Y. N., S. Kim, and R. G. Larson. 2002. Simulations of zwitterionic and anionic phospholipid monolayers. *Biophys. J.* 82:1731–1742.
43. Baoukina, S., L. Monticelli, …, D. P. Tieleman. 2007. Pressure-area isotherm of a lipid monolayer from molecular dynamics simulations. *Langmuir.* 23:12617–12623.
44. López, C. A., A. H. de Vries, and S. J. Marrink. 2011. Molecular mechanism of cyclodextrin mediated cholesterol extraction. *PLOS Comput. Biol.* 7:e1002020.
45. Evans, R. W., M. A. Williams, and J. Tinoco. 1987. Surface areas of 1-palmitoyl phosphatidylcholines and their interactions with cholesterol. *Biochem. J.* 245:455–462.
46. Phillips, L. R., M. Milescu, …, K. J. Swartz. 2005. Voltage-sensor activation with a tarantula toxin as cargo. *Nature.* 436:857–860.
47. Kučerka, N., S. Tristram-Nagle, and J. F. Nagle. 2005. Structure of fully hydrated fluid phase lipid bilayers with monounsaturated chains. *J. Membr. Biol.* 208:193–202.
48. Marsh, D. 2006. Comment on interpretation of mechanochemical properties of lipid bilayer vesicles from the equation of state or pressure-area measurement of the monolayer at the air-water or oil-water interface. *Langmuir.* 22:2916–2919.
49. Dahim, M., N. K. Mizuno, …, H. L. Brockman. 2002. Physical and photophysical characterization of a BODIPY phosphatidylcholine as a membrane probe. *Biophys. J.* 83:1511–1524.
50. Muddana, H. S., R. R. Gullapalli, …, P. J. Butler. 2011. Atomistic simulation of lipid and DiI dynamics in membrane bilayers under tension. *Phys. Chem. Chem. Phys.* 13:1368–1378.
51. Dong, Y. Y., A. C. Pike, …, E. P. Carpenter. 2015. K2P channel gating mechanisms revealed by structures of TREK-2 and a complex with Prozac. *Science.* 347:1256–1259.
52. Ge, J., W. Li, …, M. Yang. 2015. Architecture of the mammalian mechanosensitive Piezo1 channel. *Nature.* 527:64–69.
53. Evans, E., and A. Yeung. 1994. Hidden dynamics in rapid changes of bilayer shape. *Chem. Phys. Lipids.* 73:39–56.
54. Hurst, A. C., P. A. Gottlieb, and B. Martinac. 2009. Concentration dependent effect of GsMTx4 on mechanosensitive channels of small conductance in E. coli spheroplasts. *Eur. Biophys. J.* 38:415–425.
55. Perozo, E., A. Kloda, …, B. Martinac. 2002. Physical principles underlying the transduction of bilayer deformation forces during mechanosensitive channel gating. *Nat. Struct. Biol.* 9:696–703.
56. Nomura, T., C. G. Cranfield, …, B. Martinac. 2012. Differential effects of lipids and lyso-lipids on the mechanosensitivity of the mechanosensitive channels MscL and MscS. *Proc. Natl. Acad. Sci. USA.* 109:8770–8775.
57. Wieprecht, T., M. Beyermann, and J. Seelig. 2002. Thermodynamics of the coil-alpha-helix transition of amphipathic peptides in a membrane environment: the role of vesicle curvature. *Biophys. Chem.* 96:191–201.
58. Nishizawa, M., and K. Nishizawa. 2006. Interaction between K+ channel gate modifier hanatoxin and lipid bilayer membranes analyzed by molecular dynamics simulation. *Eur. Biophys. J.* 35:373–381.
59. Oswald, R. E., T. M. Suchyna, …, F. Sachs. 2002. Solution structure of peptide toxins that block mechanosensitive ion channels. *J. Biol. Chem.* 277:34443–34450.
60. Slavchov, R. I., T. Nomura, …, F. Sachs. 2014. Gigaseal mechanics: creep of the gigaseal under the action of pressure, adhesion, and voltage. *J. Phys. Chem. B.* 118:12660–12672.
61. Belyy, V., K. Kamaraju, …, S. Sukharev. 2010. Adaptive behavior of bacterial mechanosensitive channels is coupled to membrane mechanics. *J. Gen. Physiol.* 135:641–652.
62. Woody, R. W. 1994. Contributions of tryptophan side chains to the far-ultraviolet circular dichroism of proteins. *Eur. Biophys. J.* 23:253–262.
63. Ladokhin, A. S., M. E. Selsted, and S. H. White. 1999. CD spectra of indolicidin antimicrobial peptides suggest turns, not polyproline helix. *Biochemistry.* 38:12313–12319.
64. Glukhov, E., M. Stark, …, C. M. Deber. 2005. Basis for selectivity of cationic antimicrobial peptides for bacterial versus mammalian membranes. *J. Biol. Chem.* 280:33960–33967.
65. Sachs, F., and C. E. Morris. 1998. Mechanosensitive ion channels in non-specialized cells. *In* Reviews of Physiology and Biochemistry and Pharmacology. M. P. Blaustein, R. Greger, H. Grunicke, R. Jahn, L. M. Mendell, A. Miyajima, D. Pette, G. Schultz, and M. Schweiger, editors. Springer, Berlin, pp. 1–78.
66. Sukharev, S., and A. Anishkin. 2004. Mechanosensitive channels: what can we learn from 'simple' model systems? *Trends Neurosci.* 27:345–351.
67. Sukharev, S., and F. Sachs. 2012. Molecular force transduction by ion channels: diversity and unifying principles. *J. Cell Sci.* 125:3075–3083.
68. Perozo, E., D. M. Cortes, …, B. Martinac. 2002. Open channel structure of MscL and the gating mechanism of mechanosensitive channels. *Nature.* 418:942–948.
69. Corry, B., A. C. Hurst, …, B. Martinac. 2010. An improved open-channel structure of MscL determined from FRET confocal microscopy and simulation. *J. Gen. Physiol.* 136:483–494.
70. Beaven, A. H., A. J. Sodt, …, W. Im. 2015. Ion channel regulation by lipid bilayers: theory & simulation of deformed membranes around Gramicidin A. *Biophys. J.* 108:209a.

Biophysical Journal, Volume *112*

Supplemental Information

GsMTx4: Mechanism of Inhibiting Mechanosensitive Ion Channels

Radhakrishnan Gnanasambandam, Chiranjib Ghatak, Anthony Yasmann, Kazuhisa Nishizawa, Frederick Sachs, Alexey S. Ladokhin, Sergei I. Sukharev, and Thomas M. Suchyna

Methods

Fluorescence measurements of membrane binding: The interaction between these tryptophan-containing peptides and lipid vesicles was studied as described in (1). Briefly, tryptophan (Trp) fluorescence from 2 µM peptide was measured using a SPEX Flurolog FL 3-22 steady state fluorescence spectrometer (Jobin Yvon, Edison, NJ) equipped with double grating excitation and emission monochromators. Trp residues were excited at 280 nm and emission spectra were recorded between 290 nm and 500 nm using excitation and emission spectral slits of 2 and 4 nm, respectively. Measurements were made at 25°C in 2x10 mm cuvettes oriented perpendicular to the excitation beam. Quenching of Trp emission by aqueous iodide was measured in the presence of increasing concentrations of large unilamellar vesicles (LUVs) composed of either 1-palmitoyl-2-oleoyl-sn-glycero-3-phosphocholine (POPC) (Avanti, Alabaster, AL) or 25%POPC and 75% 1-palmitoyl-2-oleoyl-sn-glycero-3-phosphoglycerol (POPG). All spectra were recorded after equilibration of the sample. Corrections for background and the fitting of spectra were performed as previously described (2). Breifly, fluorescence intensities I, corrected for scattering

and dilution, were fitted to the following equation:

$$I([\mathrm{L}]) = 1 + I_{\max}\frac{K_x[\mathrm{L}]}{[\mathrm{W}] + K_x[\mathrm{L}]},$$

where I_{max} is the fluorescence increase on complete binding, [L] is the molar concentration of lipid, [W] is the molar concentration of water (55.3 M), and K_x is the mole fraction partition coefficient. The free energies of transfer from water to membrane were calculated from the mole fraction partition coefficients using

$$\Delta G = -RT \ln K_x.$$

Peptide depth estimates using aqueous and membrane resident quenchers: We used two types of quenching agents - water-soluble acrylamide and POPC:POPG vesicles made with the membrane resident 10-docylnonadecane (10-DN) quencher. Excitation and emission recording parameters were the same as above. Fluorescence was measured as increasing concentrations of the two quenching agents were added to 2 µM WT and different analog peptides.

1. Posokhov, Y. O., P. A. Gottlieb, and A. S. Ladokhin. 2007. Quenching-enhanced fluorescence titration protocol for accurate determination of free energy of membrane binding. Anal Biochem 362:290-292.
2. Ladokhin, A. S., S. Jayasinghe, and S. H. White. 2000. How to measure and analyze tryptophan fluorescence in membranes properly, and why bother? Anal Biochem 285:235-245.

CD spectrum of WT and K28E variant of GsMTx4 Peptides in Solution and Bound to Membranes

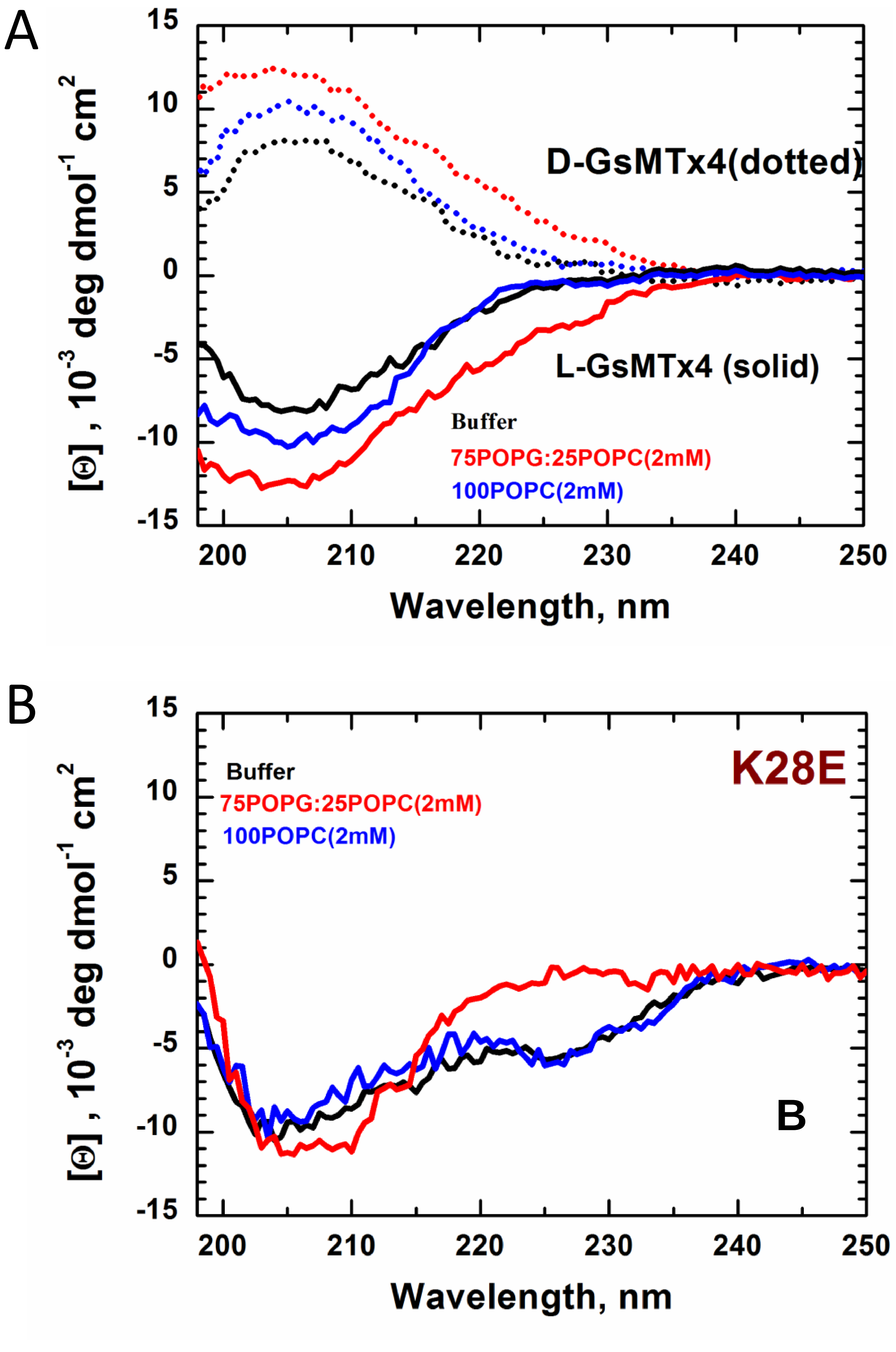

Figure S1. Representative CD spectrum of the D and L enantiomers of WT GsMTx4 (A) and the GsMTx4 K28E variant (B) in 10 mM $NaPO_4$ buffer pH 7.4, 3:1 POPG:POPC (anionic) and POPC (zwitterionic) vesicles. The negative peak at 228 nm present in the K28E variant disappears when bound to anionic, but not zwitterionic, vesicles. (n=2/peptide)

Supporting Figure S1

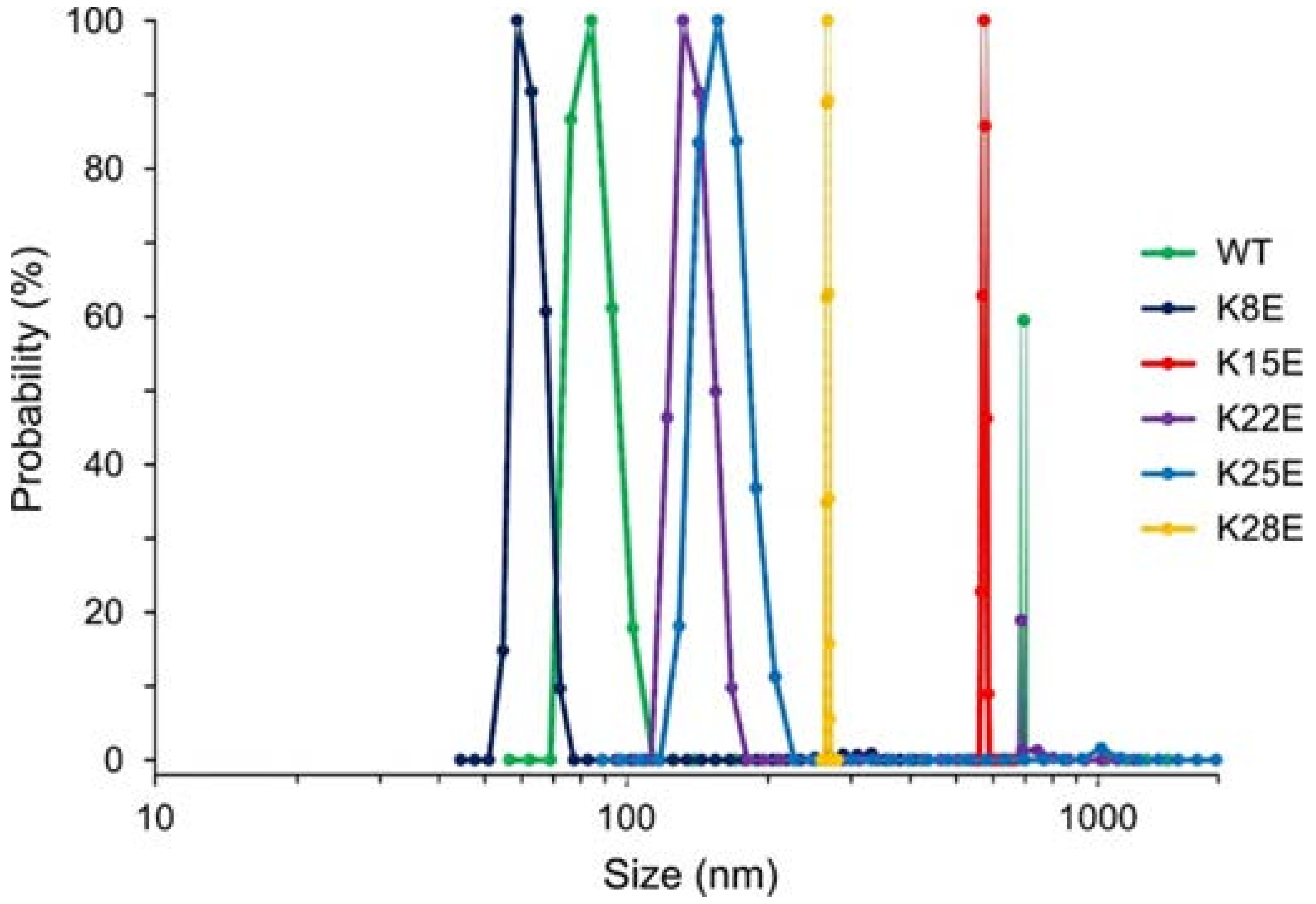

Figure S2. The distributions of particle size measured by Dynamic Light Scattering in solutions of WT GsMTx4 and four variants at 30 µM. The distributions show the K-E mutations produce different aggregation sizes for the peptides in aqueous solution. The least active peptide K15E shows the largest aggregates, while WT and the uncompromised K8E show the smallest aggregation sizes.

Dynamic light scattering analysis of peptide aggregation: Peptide aggregation is suggested by the CD results and aggregation can reduce the effective concentration (activity) of the peptide. It can also modify the partitioning of the peptide with the membrane. The aggregation properties were investigated using DLS. DLS experiments were performed with 30 µM WT or variant peptides, and the volume placed in the cuvette was 1.0 mL. All variants were tested independently three times. All peptides showed aggregate particle sizes represented by single peaks of 50-400 nm in size (Fig. 12), corresponding to aggregation numbers between 1.6×10^4 for K8E and 1.4×10^7 for the most compromised K15E variant (assuming that molecular volume of GsMTx4 is ~6.7 nm^3/monomer). Only WT and K22E peptides showed smaller peaks of larger particles near 700 nm, whereas the main peak for K15E particles was near 570 nm. It is obvious that inactive variants form larger aggregates at 30 µM which may lower the effective peptide concentration. We should note that the monomer-aggregate equilibrium is concentration-dependent (see Figure S3), but the sensitivity to aggregate sizes was too low at 3 µM. To increase the intensity of scattered light we used about an order of magnitude higher concentration than in the electrophysiological experiments.

Methods: These experiments examined the tendency of the peptides to aggregate. The peptides were diluted to 20 mM in the standard 50 mM KCl buffer and within one hour were subjected to dynamic light scattering (DLS) measurements on a 90 Plus Particle Size Analyzer (Brookhaven Instruments Corp.) pre-calibrated with 92nm nanospheres (Duke Scientific Corp.). Autocorrelation data were collected during five 1-min intervals and averaged.

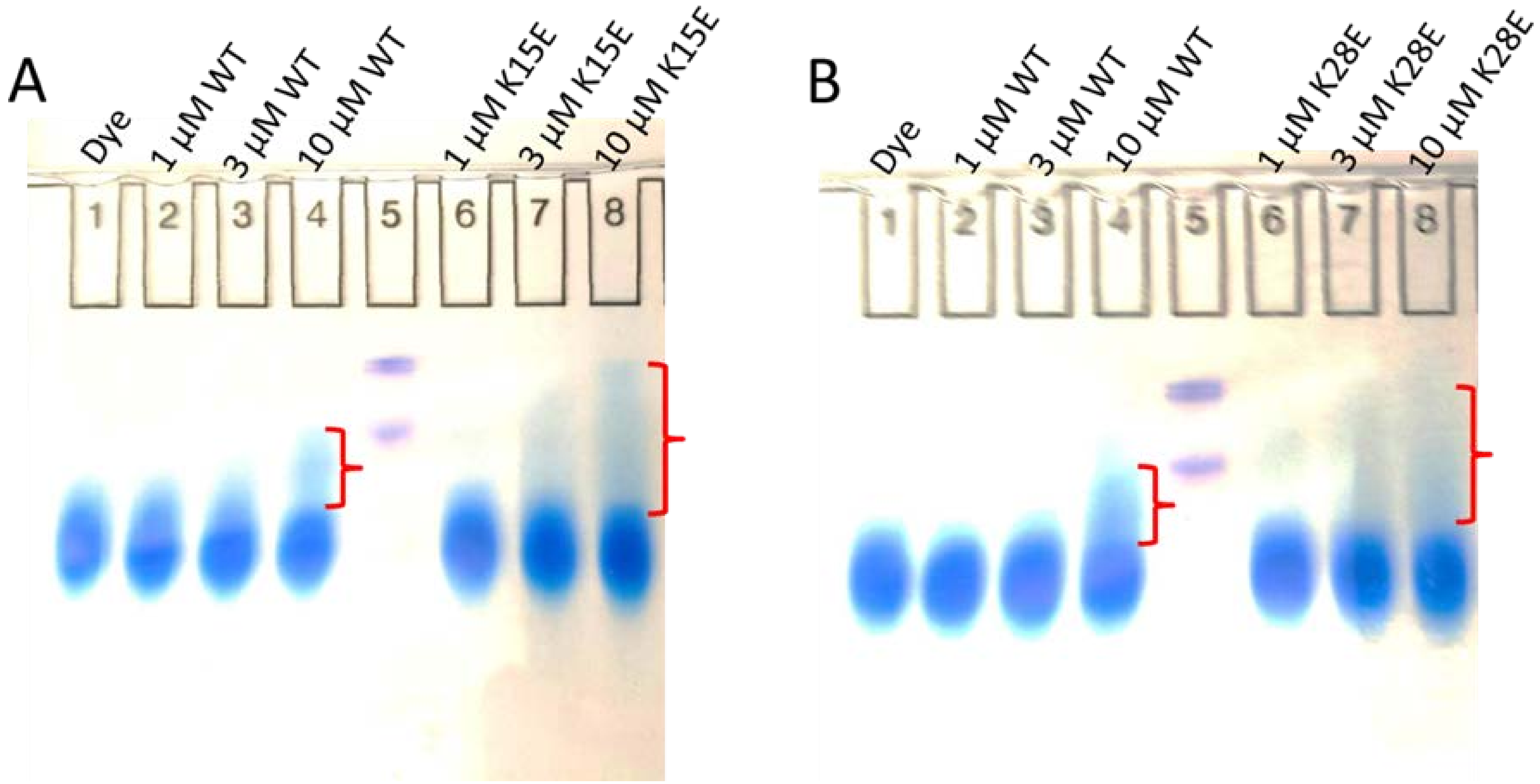

Figure S3. GsMTx4 WT and either K15E (A) or K28E (B) variants run by nondenaturing PAGE suggesting peptide aggregation at higher concentrations. Three concentrations for each peptide show that aggregate size increases with concentration, and that the aggregate sizes are larger for the variants than WT (red brackets). However, at 1 µM there is little evidence of aggregation. This is not due to sensitivity since we are able to detect <10 ng of protein with G250 dye (1 µM = 40 ng of protein in 10 µl).

Non-denaturing gel electrophoresis analysis of peptide aggregation: To determine the concentration dependence of aggregation size at lower concentrations, we ran WT, K15E, and K28E at 1, 3, and 10 µM on non-denaturing gels to estimate particle sizes. SDS denatured samples of 10 µM WT and variant peptides dissociated into the 4096 Da monomeric form and all material ran with G250 dye in the loading buffer. However, under non-denaturing conditions we observed results similar to those observed in the DLS experiments, where larger aggregates (slowly migrating) were present for the variants compared to the WT peptide (Fig. S3). Aggregate sizes were concentration dependent with no visible aggregates detected at 1 µM (40 ng of peptide), and only weakly retarded species at 3 µM. Significantly larger aggregates were observed at 10 µM. Due to the non-denaturing conditions we were unable to determine the aggregate sizes, but clearly some aggregation is occurring at lower concentrations and users should be mindful of this property.

Methods: : Three concentrations (1, 3 and 10 µM) of WT peptide and variant peptides (K8E and K28E) were run on 10-20% gradients of Tris/Tricine polyacrylamide gels from Biorad. The gels were run at 100 V and 400 mA for 1 hour. The markers were Precision Plus dual extra protein standard marker from Biorad containing SDS. Tris Tricine running buffer contained 100 mM Tris and 100 mM Tricine at pH 8.3. Tricine loading buffer contained 100 mM TrisCl, pH 8.3, 30% glycerol, and 0.25% Coomassie Brilliant blue G 250. The G250 stain is sensitive to 10 ng of protein.

Supporting Figure S3

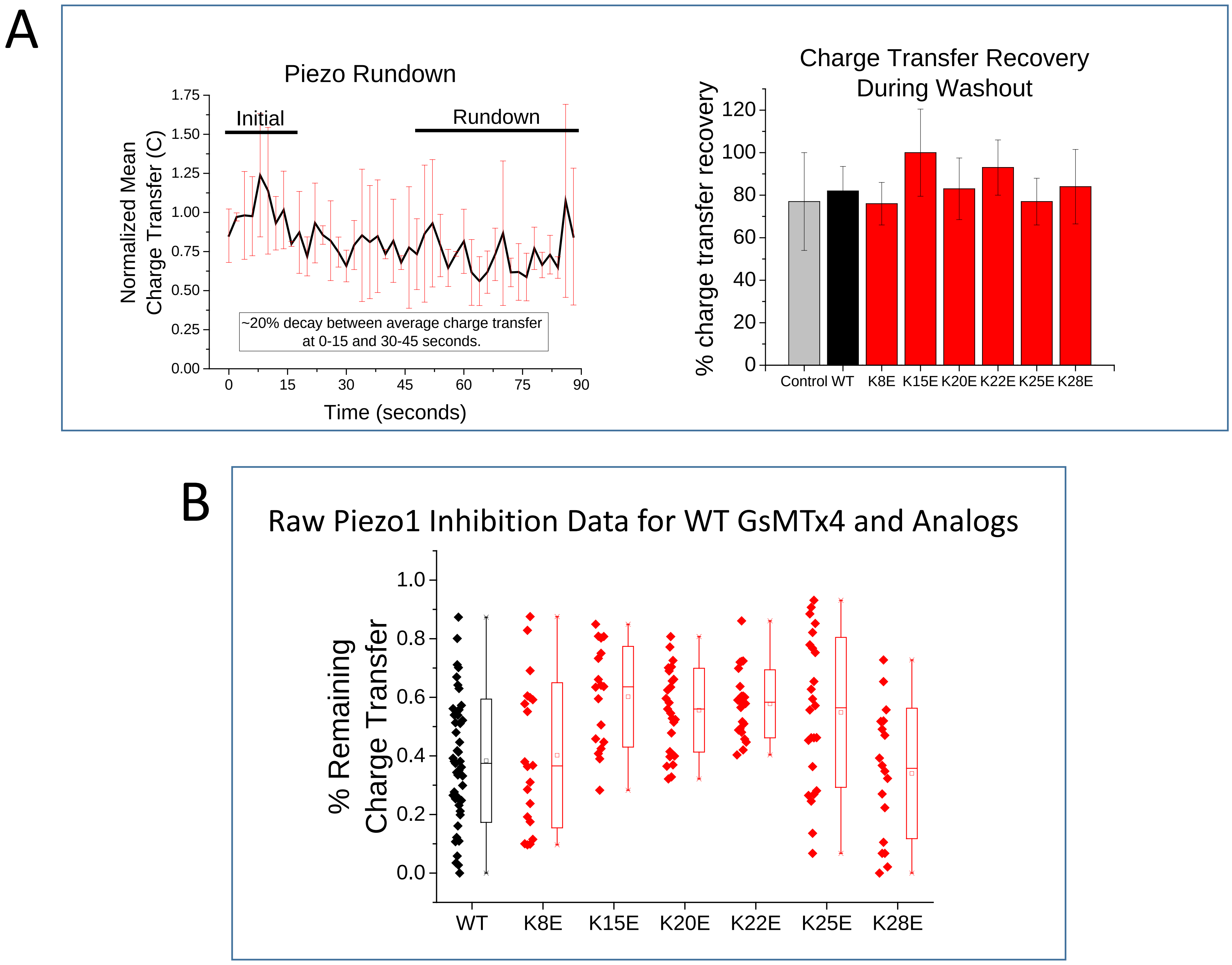

Figure S4. Summary of channel rundown, recovery and inhibition strength from peptide application. (**A**) The trace in the left panel shows the mean charge transfer from n=3 patches in normal saline expressing piezo channels monitored over 1.5 min to determine the rate of rundown. Pressure steps were applied every 2 seconds. The mean charge transfer over the first 20s (*Initial* black line) was set as 100% and the amount of rundown was assessed by normalizing the charge transfer that occurred between 60-90s (*Rundown* black line) to this initial level. The bar graph in the right panel shows there was ~20% rundown over 75 seconds which is shown by the control (gray) bar. Most tests of peptide inhibition on Piezo channels took ~75 seconds for the decay and recovery phases to be measured. The recovery levels after washout of the different peptide analogs was consistent with this level of rundown in the control patches. (**B**). The time for application and washout generally took 60-90 seconds and the levels of charge transfer recovery following washout of the different analogs were similar to the control level. This suggests that nearly complete washout of the peptides occurred after 20 seconds of wash time. (**C**) Summary of percent charge transfer reduction for all patches used in the inhibition potency tests of WT (black) and analog (red) peptides. Box plots for each peptide tested were generated from the fractional remaining steady state decay current for each patch shown to the left of the boxes (number of patches for each peptide were WT=47, K8E=20, K15E=18, K20E=25, K22E=22, K25E=24, K28E=18). The ends of the boxes represent 1 SD from the mean designated by (▫). The line through the box is the median and the extended lines ended with x at the ends designate the range of the data.

Supporting Figure S4

k_{a2} slower rate constants from decay fits

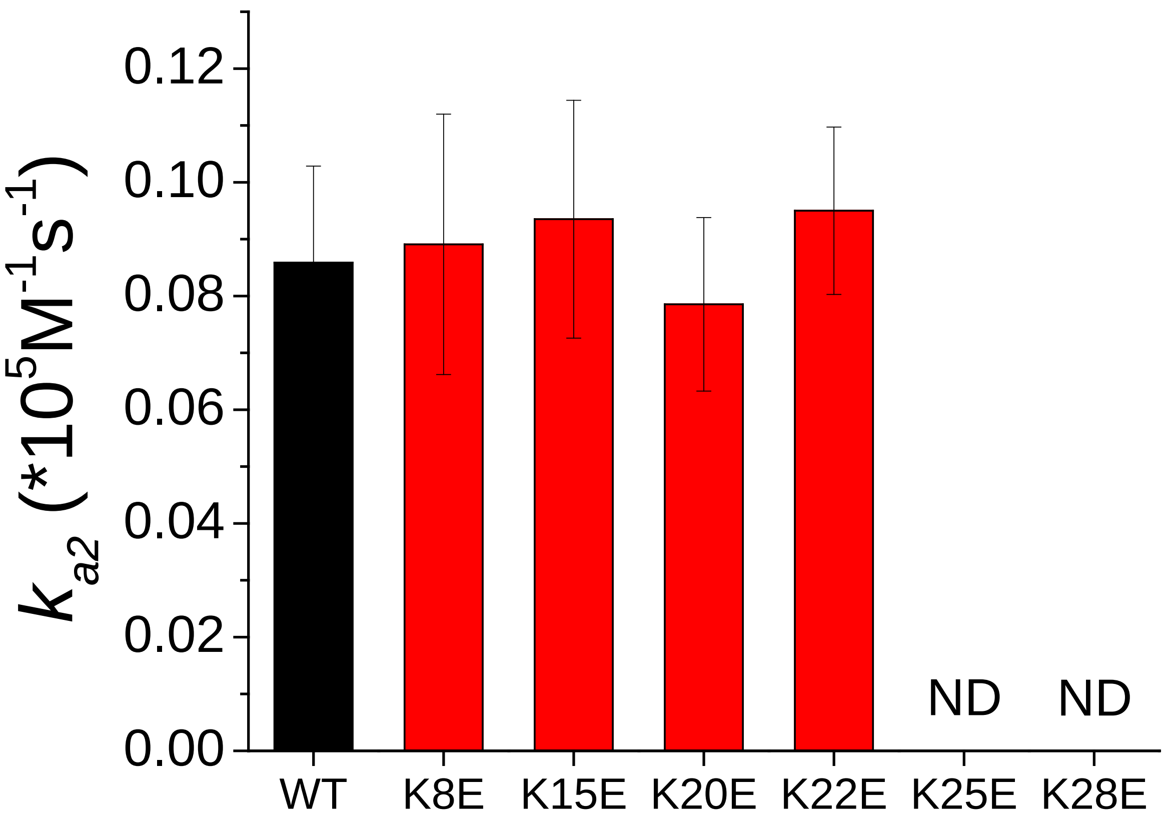

Figure S5. For all peptides, >50% of patch data showed current decays that were modeled best using two time constants as shown in Fig. 2C. The k_a values calculated from the second (slower) decay time constant shows no difference between the variants and WT peptide. The number of patches for each peptide were WT=15, K8E=12, K15E=12, K20E=16, K22E=12). K25E and K28E were not determined (ND) because too few patch data sets produced acceptable fits for the second time constant.

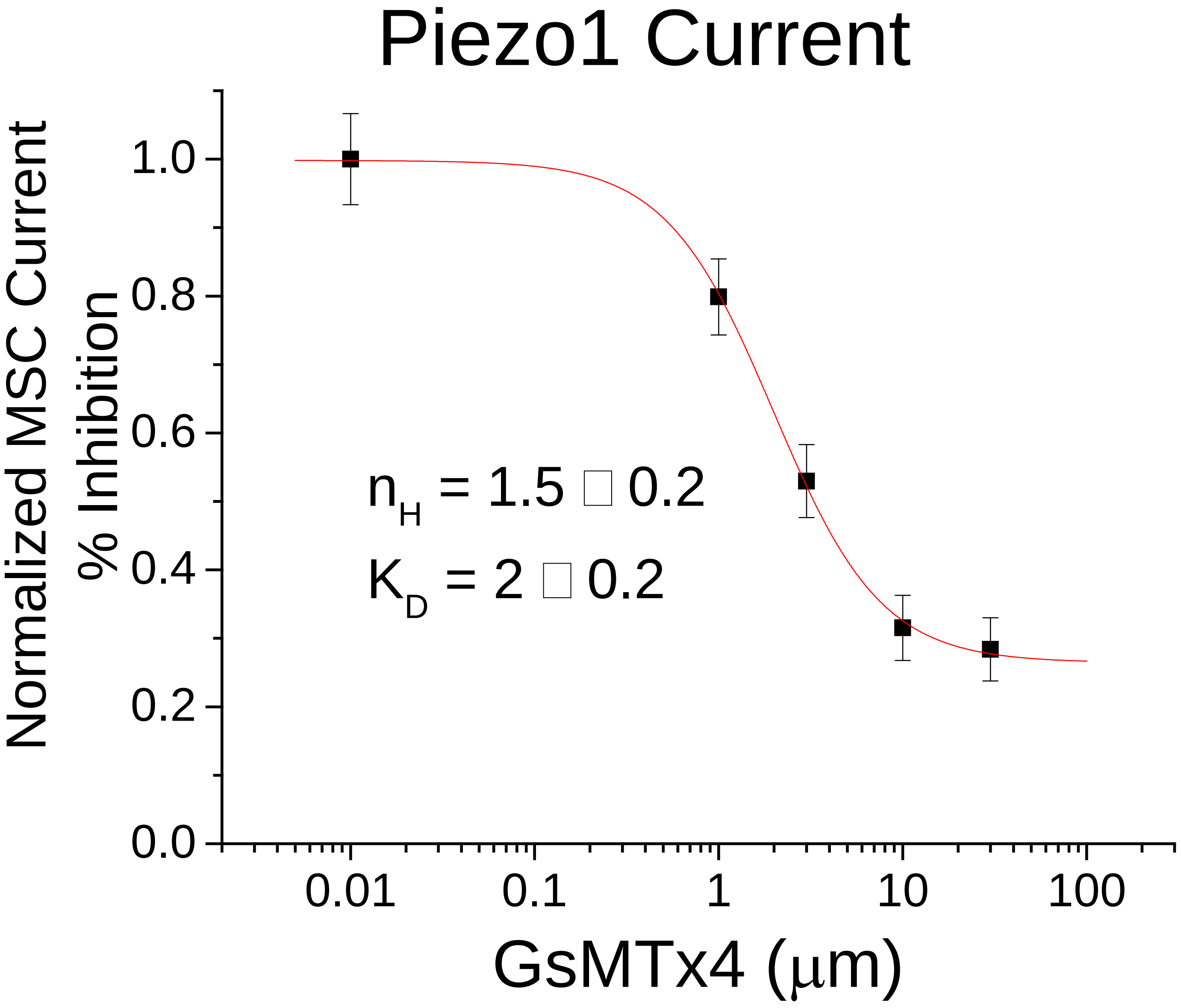

Figure S6. Concentration dependence of inhibition by WT GsMTx4. Each point represents the average Piezo1 current from 7-12 patches in the presence of the indicated GsMTx4 concentration. Red curve shows the Hill equation fit to the data. The K_D's determined here are slightly higher than the previously determined K_D (~0.5 µM) (1,2) likely due to differences in the pressure step protocols used in the different studies. The Hill coefficient was 1.5, suggesting that inhibition may involve more than one peptide. Interestingly, MD simulations predict that stable dimer formation occurs at resting tension between a membrane bound and a second unbound GsMTx4 peptide, and that the second peptide dissolves rapidly into the membrane upon an increase in tension (3).

1. **Suchyna, T. M., J. H. Johnson, H. F. Clemo, Z. H. Huang, D. A. Gage, C. M. Baumgarten, and F. Sachs. 2000. Identification of a peptide toxin from Grammostola spatulata spider venom that blocks stretch activated channels. Journal of General Physiology 115:583-598.**
2. **Bae, C., F. Sachs, and P. A. Gottlieb. 2011. The mechanosensitive ion channel Piezo1 is inhibited by the peptide GsMTx4. Biochemistry 50:6295-6300.**
3. **Nishizawa, K., M. Nishizawa, R. Gnanasambandam, F. Sachs, S. I. Sukharev, and T. M. Suchyna. 2015. Effects of Lys to Glu mutations in GsMTx4 on membrane binding, peptide orientation, and self-association propensity, as analyzed by molecular dynamics simulations. Biochimica et Biophysica Acta (BBA)-Biomembranes.**

TREK1 Currents Potentiated by GSMTx4

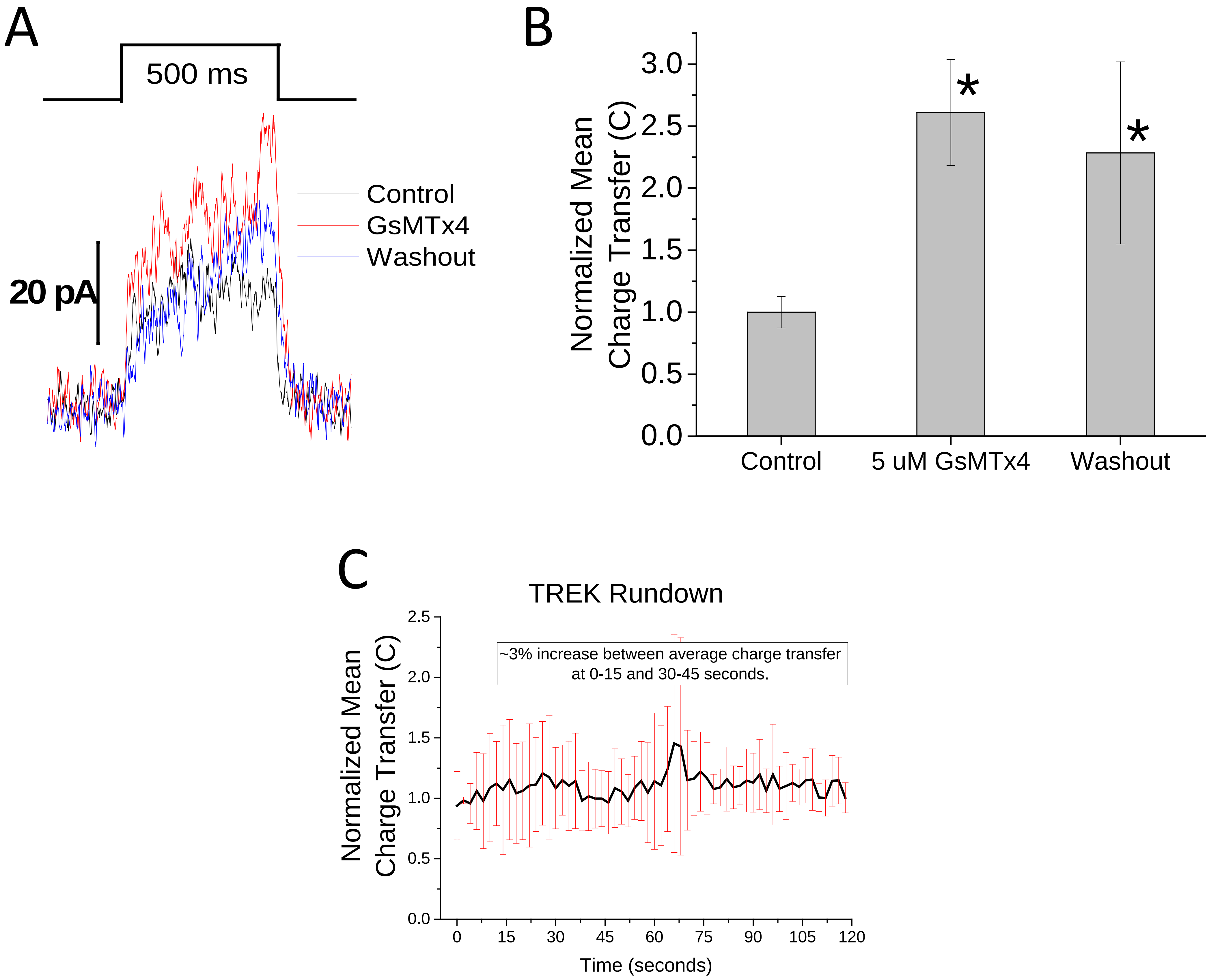

Figure S7. TREK1 channel currents are potentiated by GsMTx4. TREK 1 currents from HEK cell outside-out patches were observed in increase when 5 µM GsMTx4 was applied **(A)**. Representative traces show TREK1 currents did not inactivate during a pressure step and were also active during the intervening unstretched time between pressure steps as shown by the greater noise level of the baseline compared to Piezo1 currents in Figure 2. GsMTx4 produced an average 2.6±0.06 fold increase in activity (n=6 patches) that did not decrease significantly after 60 seconds of washout **(B)** (* denotes significantly different from control current at α = 0.05). **(C)** Mean charge transfer from three TREK 1 expressing patches showed no rundown over two minutes of constant stimulation in normal bath saline.

Methods: HEK293 cells were transfected with 0.5-1 µg of TREK cDNA expression vector containing a GFP indicator of transfection. For recordings of TREK channels, the bath solution contained (in mM): 150 KCl, 1 $CaCl_2$, 1 $MgCl_2$, 10 HEPES and the pipette solution contained 150 KCl, 10 HEPES. The pH of these TREK channel recording solutions were adjusted to 7.4. We used protocols identical to those used for activation of Piezo channels to activate TREK channels; they were activated at 50 mV and 40-90 mmHg.

Supporting Figure S7

Peptide-vesicle affinity determined by isothermal titration calorimetry:

Peptide	N1	K1 (M^{-1})	ΔH1 (Cal/mol)	ΔS1 (Cal/mol·K)	N2	K2 (M^{-1})	ΔH2 (Cal/mol)	ΔS2 (Cal/mol·K)
L-GsMTx4	1.9±0.6	(2.4±1.2)E5	-1078±470	21.2±2.0	2.4±0.9	(2.7±1.6)E6	-1565±96	24.2±0.8
K8E	0.4±0.1	(8.0±3.2)E4	-1580±80	17.2±2.2	0.8±0.2	(8.8±1.6)E6	-1530±120	26.6±1.2
K15E	0.2±0.1	(8.6±4.3)E6	5150±2020	63±20	0.8±01	(2.2±1.2)E7	-5073±480	16.5±1.0
K22E	1.9±0.8	(2.3±1.6)E5	-934±202	21.5±1.4	3.1±1.1	(5.4±3.6)E6	-1500±20	25.8±0.2
K25E	1.4±0.2	(2.4±1.1)E5	-448±257	20.1±3.2	2.4±1.2	(3.1±1.1)E7	-773±110	28.6±3.2
K28E	1.3±0.5	(8.3±3.2)E5	-690±180	23.2±1.8	0.9±0.3	(2.1±0.7)E7	-903±85	30±0.7

Table S1. ITC Fitting Parameters. Based on the density values (N1 and N2), the low- and high-affinity sites occur in comparable amounts/densities. Of the two most compromised variants, K25E shows the highest K_2, and the K15E has positive ΔH1 and high ΔS1 suggesting that the low-affinity binding mode is different for this variant. The high-affinity binding mode for K15E variant is also characterized by unusually large negative enthalpy ΔH2. Each titration was repeated at least 3 times. The parameters are shown as mean ± SD.

Supporting Data Table S1

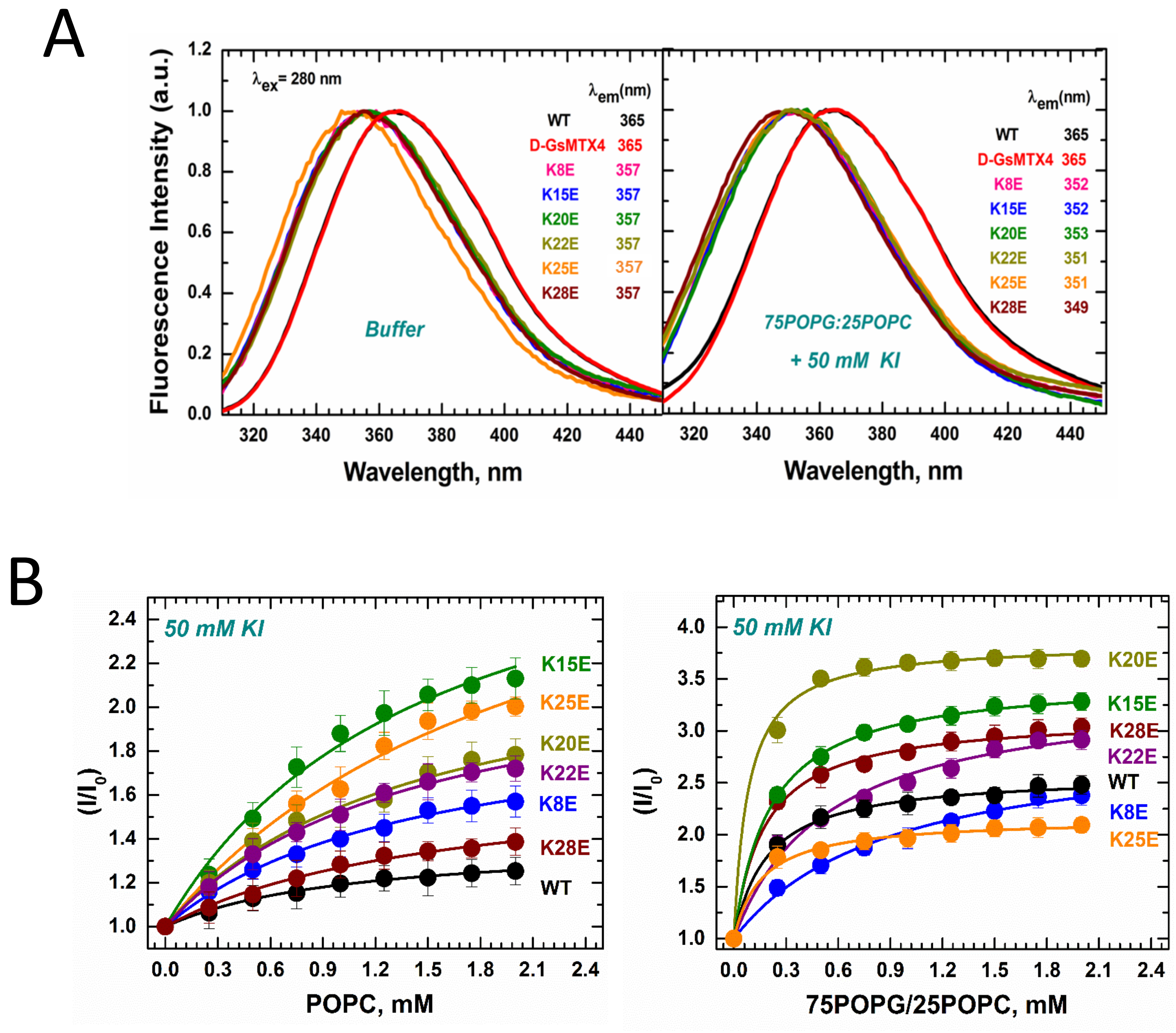

Figure S8. (A) Representative tryptophan fluorescence spectrums for GsMTx4 WT and K-E variants in solution (peptide concentration 2 µM) containing KI (first panel) and in the presences of 75POPG:25POPC LUVs (n=2 tests per variant). All variants had a pronounced ~8 nm blue shift compared to the D and L enantiomeric WT forms of GsMTx4 in solution. The blue shift for the variants was even more pronounced when bound to the POPG-POPC vesicles, but the WT peptides were unaffected. **(B)** Shows Trp fluorescence intensity curves for the different peptides titrated using increasing concentration of POPC or POPG-POPC LUV in the presence of aqueous 50 mM KI (n=3/variant). As the LUV concentration increases, peptide association with the membrane increases leading to protection of Trp quenching by aqueous iodine. Significantly higher concentrations of zwitterionic POPC LUV are required (first panel) to titrate the KI quenching compared to anionic POPG-POPC LUVs (second panel), and maximum protection levels for POPG:POPC were greater. Fitting of the titration data with a partitioning model suggests that the free energy of partitioning ΔG for all variants were similar to that of WT GsMTx4 for either LUV composition, but the values of the final intensity increase (Imax) were generally higher in variants suggesting lesser accessibility of Trps to quencher in membrane bound state.

Lipid titration of Trp quenching: GsMTx4 has two adjacent Trp residues that have a peak emission intensity at 365 nm in solution and were unaffected by binding to LUVs (Fig. S8A). The K-E variants all showed a peak emission intensity that was blue shifted ~8nm from WT in solution, suggesting a common effect of net charge on the Trp's environment. The blue shift is correlated with a more hydrophobic environment which, in solution, likely represents enhanced peptide aggregation that partially shields the Trp residues from the aqueous environment (see enhanced aggregation in Supporting Figs. S2 and S3). As shown previously (1), both the D and L enantiomers of WT GsMTx4 were not blue shifted in the presence of either POPC or POPG-POPC LUVs (Fig. S8A, second panel and Table S2). The variants all showed a blue shift in the presence of POPG-POPC LUV, but not POPC (Supporting Fig. S8A and Table S2). We suggested that the lack of blue shift for the WT and D-enantiomer may be related to incomplete dehydration of the Trp residues upon binding (1). The presence of the shift for the variants in anionic vesicles suggests a more hydrophobic environment for the Trps, possibly related to a deeper penetration than WT.

The significant differences in I_{max} for the different peptides may represent differences quenching between membrane bound and aggregate fractions, or differences in peptide tilt, penetration depth and local lipid packing. There was a general trend for most variants to have higher I_{max} values than WT.

1. Posokhov, Y. O., P. A. Gottlieb, and A. S. Ladokhin. 2007. Quenching-enhanced fluorescence titration protocol for accurate determination of free energy of membrane binding. Anal Biochem 362:290-292.
2. Suchyna, T. M., J. H. Johnson, H. F. Clemo, Z. H. Huang, D. A. Gage, C. M. Baumgarten, and F. Sachs. 2000. Identification of a peptide toxin from Grammostola spatulata spider venom that blocks stretch activated channels. Journal of General Physiology 115:583-598.

Peptides	Fluorescence λ_{max} (nm) （± 1 nm）			ΔG, kJ/mole		I_{max}		Z_{eff}
	Buffer	100% POPC	75% POPG 25% POPC	100% POPC	75% POPG 25% POPC	100% POPC	75% POPG 25% POPC	
L-GsMTx4	365	365	365	-26.9 ± 0.3	-31.1 ± 0.2	1.4 ± 0.1	2.6 ± 0.1	+0.5
K8E	357	357	352	-26.2 ± 0.3	-27.3 ± 0.3	2.0 ± 0.1	3.0 ± 0.1	+0.2
K15E	357	357	352	-26.1 ± 0.4	-30.9 ± 0.1	3.1 ± 0.2	3.5 ± 0.1	+0.5
K20E	357	357	353	-26.2 ± 0.5	-33.3 ± 0.4	2.3 ±0.2	3.8 ± 0.1	+0.8
K22E	357	357	351	-26.2 ± 0.5	-28.6 ± 0.3	2.3 ±0.1	3.4 ± 0.1	+0.3
K25E	357	357	351	-25.1 ± 0.5	-31.6 ± 0.4	3.2 ±0.2	2.2 ± 0.1	+0.7
K28E	357	357	349	-25.9 ± 0.4	-31.4 ± 0.3	1.7 ±0.1	3.2 ± 0.1	+0.6

Table S2. Trp fluorescence changes associated with K-E variants and vesicle binding (partitioning model fitting parameters = means ± SE, n=3/peptide).

Supporting Table S2

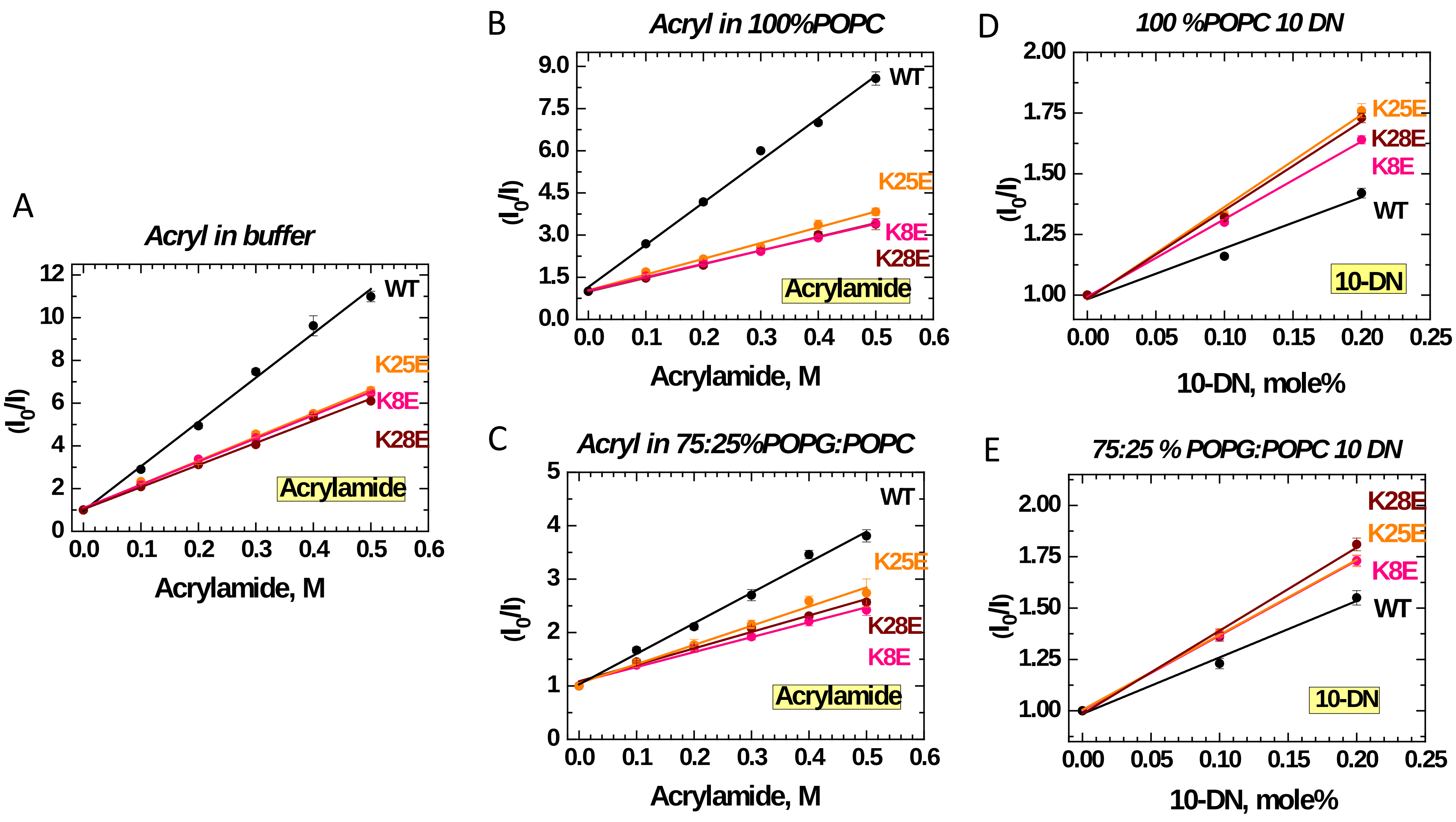

Figure S9. Acrylamide versus 10-DN quenching (K_{SV}) was used to compare penetration depth of WT and three different K-E variants at 2 µM peptide. (A) Shows the ratio of the initial fluorescent intensity to the quenched intensity (I_o/I, means±SE) for WT GsMTx4, and K8E, K25E, and K28E variants vs the concentration of Acrylamide (λ_{ex} = 295 nm). Spectra for these peptides in the presence of either 100% POPC (B) or 75%POPG:25%POPC (C) are corrected for the inner filter effect determined in buffer alone. The quenching is linearly related to the quenching agent concentration. The color coded KSV values in buffer and in the presence of the different types of LUVs is shown above the quenching data. The I_o/I for WT and variant peptides vs the concentration of the bilayer resident 10-DN quenching agent (λ_{ex} = 280 nm) is shown for POPC (D) and POPG/POPC (E) vesicles. At these concentrations quenching is linearly related to the concentration. All data sets are from n=3 tests.

Peptides	Buffer	Acrylamide 100%POPC	Acrylamide 75:25% POPG:POPC	10-DN 100%POPC	10-DN 75:25% POPG:POPC
WT	**20.8 ± 0.7**	**15.0 ± 0.5**	**5.7 ± 0.2**	**2.1 ± 0.3**	**2.8 ± 0.3**
K8E	**10.8 ± 0.2**	**4.7 ± 0.1**	**2.8 ± 0.1**	**3.2 ± 0.1**	**3.7 ± 0.3**
K25E	**11.1 ± 0.3**	**5.6 ± 0.2**	**3.6 ± 0.2**	**3.8 ± 0.2**	**3.7 ± 0.1**
K28E	**10.3 ± 0.3**	**4.9 ± 0.1**	**3.1 ± 0.2**	**3.7 ± 0.3**	**4.1 ± 0.3**

Table S3. Stern-Volmer quenching constant (KSV) calculated from the slopes of Trp fluorescence quenching data in Fig. S9. KSV values for water the soluble quencher acrylamide are expressed in units of M-1 and for membrane soluble 10-DN in dimensionless units. All values are means±SE (n=3) with * denoting statistically different Stern-Volmer constants from WT (α = 0.05).

Peptide depth analysis: Dual quenching analysis of peptides with two different quenching agents residing either in solution or in the membrane was compared to the brominated lipid method (Fig. S9). Acrylamide was the *aqueous* quencher that is unable to quench the fluorescence of residues deeply embedded in the bilayer (Fig. S9A, B and C). The other is 10-doxylnonadecane (10-DN) that is hydrophobic and efficiently quenches Trp residues residing near the bilayer center. The slope of the plot of quenching agent concentration vs the ratio of quenched fluorescence is the Stern-Volmer quenching constant (K_{SV}).

Trp fluorescence decreased linearly as the concentration of acrylamide increased in saline (Fig. 9A), or when peptides were bound to LUVs of POPC (Fig. 9B) or POPG-POPC (Fig. 9C). Quenching was greater in saline than in the presence of vesicles confirming membrane binding. ***However, the variants also showed significantly greater quenching in solution.*** The sensitivity of Trp fluorescence to 10-DN incorporated in POPC (Fig. 9D) and POPG-POPC (Fig. 9E) was also concentration dependent, but with a much shallower slope. Comparing the quenching constants of the three K-E variants to WT in the membrane-bound state (Table S3) shows that the variants have lower accessibility for water-soluble acrylamide and higher accessibility to membrane-soluble 10-DN suggesting increased shielding of variant Trp residues. However, Trp fluorescence in the variants is more strongly shielded in solution (likely due to greater aggregation), and this may contribute to the significantly greater shielding in the presence of lipids. Aggregation shielding contributions may exaggerate the difference between the variants and WT peptide and making it difficult to interpret the depth differences by this method.

Supporting Figure S9 and Table S3

Membrane Area Occupied by WT and Variant Peptides

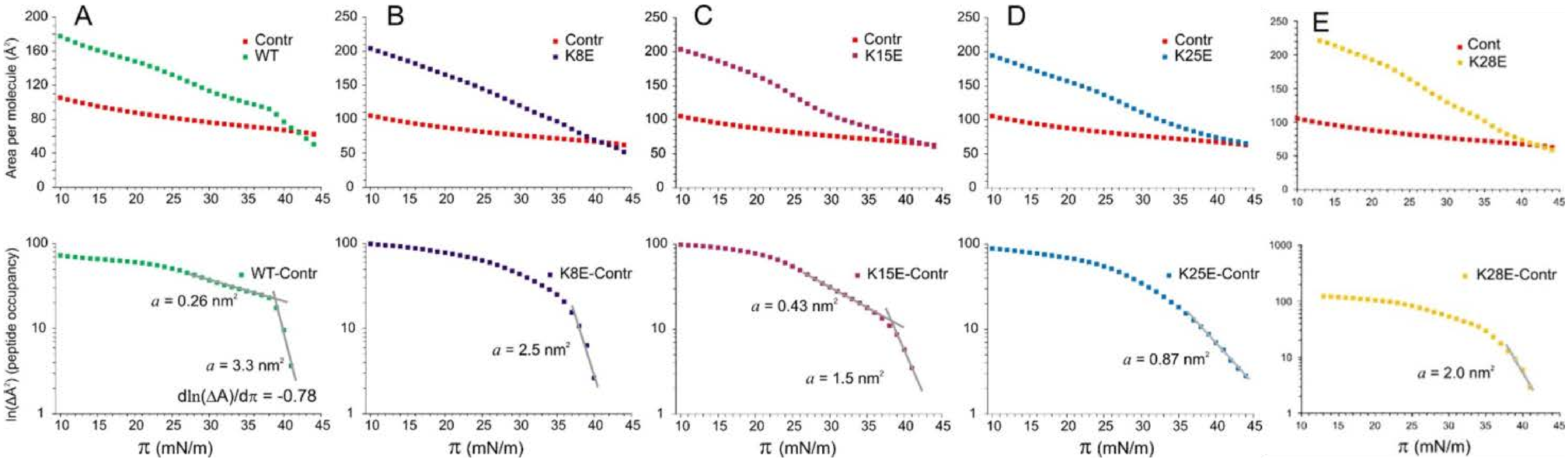

Figure S10. Plots of the area vs pressure (top panels) between the control and peptide curves for WT (A), normal activity variants K8E (B) and K28E (E), and the two least active variants K15E (C) and K25E (D). These plots illustrate partitioning of peptides into the monolayer in the expanded state (low pressures) and expulsion back to the subphase at higher pressures. The WT isotherm intersects with the control monolayer near the πB, while the least active variant isotherms approach the control near the πB but never intersect. Conversion to the logarithm of the area vs pressure (bottom panels) provides a clearer representation of the transitions during compression. If we assume that the change of the log-area with increasing pressure represents either the displacement of the peptide to a shallower state or complete expulsion of the peptide to the subphase, the slope of the film compaction can be used to calculate the peptide contribution to cross-sectional area prior to the transition. The active peptides (A, B and E) are displaced by lateral pressure from positions with effective molecular areas of 3.4 ± 0.1, 3.0 ± 0.2 and 2.3 ± 0.2 nm², whereas the transitions in inactive peptides (C and D) are shallower and show smaller molecular area changes.

The peptide intercalated into the film takes up substantial area and its presence is evident in expanded films. Compaction of the monolayer by the barrier and increase of lateral pressure leads to partial expulsion of the peptide back to the solution. To visualize the area occupied by the peptide we re-plotted the pressure-area curves in area-pressure coordinates and presented the area difference in log scale (Fig. S10). Assuming that the area change is proportional to the probability of a peptide inserting into lipid p_{lip} while p_{bulk} (concentration in the bulk) is constant, one can write

$$K_{eq} = \frac{p_{lip}}{p_{bulk}} = e^{-(\Delta G + \pi a)/kT} \quad , \quad \text{so that} \qquad kT(\ln p_{lip} - \ln p_{bulk}) = -\Delta G - \pi a$$

Differentiating with respect to π we obtain,

$$-kTd(\ln p_{lip})/d\pi = a$$

where a is the area occupied by the peptide molecule in the plane of the lipid film.

The bottom row in Figure S10 is a plot of the log of the area difference vs pressure for the WT and four variants with a range of inhibitory properties. The obvious difference between WT, K8E, and K28E, and the two weakened activity peptides is the character of the intersection of the corresponding isotherms with the control. The slope of the logarithmic difference area plot near that intersection also reflects that difference. The flattening of the isotherms for active peptides occurring in the vicinity of the πB is the property that means high compressibility in that region.

For WT GsMTx4 (Fig. S10, bottom panel), one can see that there is minimal total area change at pressures below 20 mN/m. However, above 20 mN/m, the monolayer with the peptide starts compacting faster showing two compaction rates. A shallow-slope, or "*slow expulsion*" with an area change of 0.26 nm² is observed at pressures between 25-37 mN/m. At 37mN/m the WT-harboring monolayer undergoes a sharp transition reflecting a massive displacement/expulsion of the peptide. The slope corresponds to a particle with a cross-sectional area a = 3.4± 0.1 nm². The two variants with normal activity (K8E and K28E) also show relatively large changes in cross-sectional area. In contrast, no sharp transitions were observed in compromised K15E or K25E, but near the πB, particles were effectively displaced with the slopes corresponding to smaller characteristic areas between 2.8 ± 0.4 and 0.82 ± 0.9 nm², respectively. Figure S10 D shows that the K25E variant is apparently not completely expelled as its isotherm shallowly approaches the control curve but never crosses it.

Supporting Figure S10

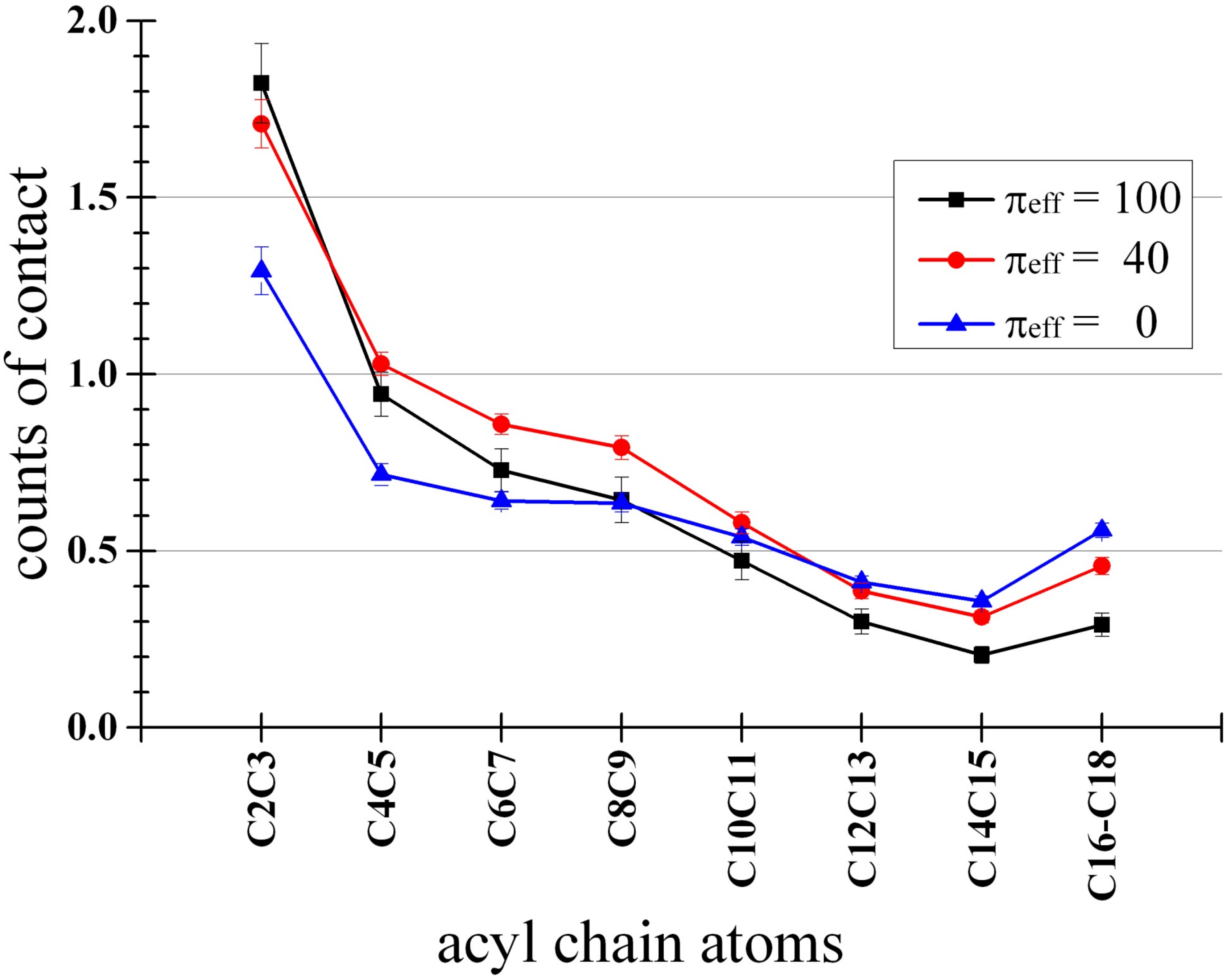

Figure S11. Simulation analysis of penetration depth of WT in the POPC monolayer based on the number of acyl chain (united) atoms in contact with WT. The y-axis shows the mean counts of the POPC acyl chain atoms (indicated in the x-axis) that were located within 3Å from any atoms of WT in the monolayer simulation data analyzed in Figure 7. Results for three distinct target membrane pressures (π_{eff}=0, 40 and 100) were shown. 'C2C3', for example, stands for the sum of the counts for C2 and C3. Error bars represent s.e. from the final 20ns of the trajectories.